# Instability waves in a subsonic round jet detected using a near-field phased microphone array

By T A K A O  S U Z U K I† A N D  T I M  C O L O N I U S

Division of Engineering and Applied Science, California Institute of Technology,
Pasadena, CA 91125, USA

We propose a diagnostic technique to detect instability waves in a subsonic round jet using a phased microphone array. The detection algorithm is analogous to the beam-forming technique, which is typically used with a far-field microphone array to localize noise sources. By replacing the reference solutions used in the conventional beam-forming with eigenfunctions from linear stability analysis, the amplitudes of instability waves in the axisymmetric and first two azimuthal modes are inferred. Experimental measurements with particle image velocimetry and a database from direct numerical simulation are incorporated to design a conical array that is placed just outside the mixing layer near the nozzle exit. The proposed diagnostic technique is tested in experiments by checking for consistency of the radial decay, streamwise evolution and phase correlation of hydrodynamic pressure. The results demonstrate that in a statistical sense, the pressure field is consistent with instability waves evolving in the turbulent mean flow from the nozzle exit to the end of the potential core, particularly near the most amplified frequency of each azimuthal mode. We apply this technique to study the effects of jet Mach number and temperature ratio on the azimuthal mode balance and evolution of instability waves. We also compare the results from the beam-forming algorithm with the proper orthogonal decomposition and discuss some implications for jet noise.

## 1. Introduction

Large-scale structures in turbulent jets are often qualitatively associated with Kelvin–Helmholtz instabilities of the inflectional mean-velocity profile (Crighton & Gaster 1976; Mankbadi & Liu 1981). In acoustically excited jets, pressure and velocity fluctuations have been successfully predicted using eigenfunctions obtained from linear stability analysis (Zaman & Hussain 1980; Mankbadi 1985; Tam & Morris 1985; Tanna & Ahuja 1985). While large-scale coherent structures reminiscent of instability waves have also been observed in natural jets (Brown & Roshko 1974; Michalke & Fuchs 1975; Maestrello & Fung 1979; Morris, Giridharan & Lilley 1990; Arndt, Long & Glauser 1997; Jordan *et al.* 2004; Hall, Pinier & Glauser 2006), it is difficult to assert whether they can be quantitatively identified with instability waves. One difficulty stems from a lack of time-resolved three-dimensional flow measurements, which are necessary for such an identification. A second and more fundamental difficulty is that turbulence in the jet consists of eddies with a range of length scales and lifetimes; thereby, it is unclear whether there is an appropriate scale-separation

† Present address: Graduate School of Engineering, University of Fukui, Fukui, 910-8507, Japan.
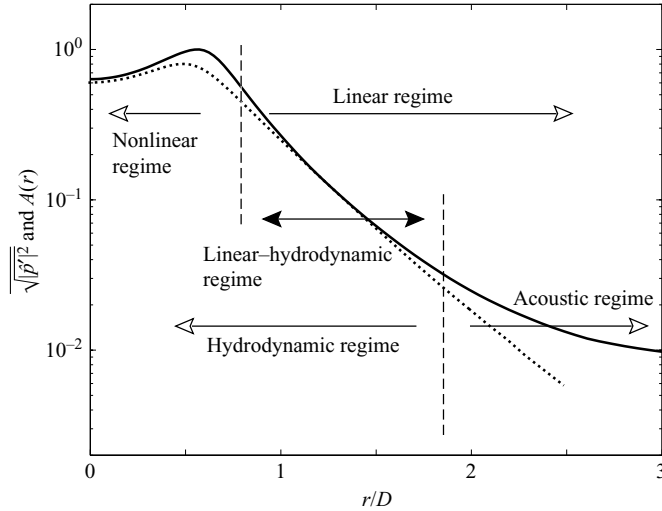
FIGURE 1. Diagram of the flow regimes of a round jet in the radial direction. The solid line depicts the time-averaged pressure fluctuation of the axisymmetric mode (i.e. $m = 0$) at $x/D = 4$ from DNS (Freund 2001), and the dotted line denotes the corresponding eigenfunction calculated from linear stability analysis. The maximum pressure fluctuation is normalized as unity, and the eigenfunction is arbitrarily scaled.

that allows instability waves to evolve in the time-averaged flow without interaction with smaller-scale turbulence. The instability waves in natural jets are correlated over shorter distances and time scales than those in forced jets. Hence, even if the detailed three-dimensional flow field were available, there are no existing techniques that would permit a decomposition of the nonlinear field into separate contributions from instability waves and other disturbances.

The difficulty associated with decomposition of the turbulent near field can be alleviated by measuring fluctuations just outside the jet mixing layer, where the pressure signals are governed by the linear wave equation. If instability waves are present in the jet, they must be accompanied by an evanescent pressure field, which is exponentially decaying with radius in this region (see the *linear hydrodynamic regime* in figure 1). At the low frequencies typically associated with instability waves, nonlinear pressure fluctuations from smaller-scale turbulence tend to decay more rapidly with radius. Moreover, acoustic waves generated by the turbulence are likely to be of smaller amplitude, although they decay more slowly. In §2.1, we provide detailed estimates for these decay rates and conclude that at low frequencies, there exists a region where the evanescent pressure field associated with linear instability waves should dominate the total pressure fluctuations. This allows us to project pressure signals onto the known solution (i.e. eigenfunctions representing instability waves) and to infer the amplitude of instability waves.

Thus, the goal of the present work is to acquire pressure signals just outside the mixing layer and to determine whether the evanescent pressure field is consistent with instability waves evolving in the time-averaged turbulent jet flow. To this end, we propose using a phased microphone array surrounding the jet from the nozzle exit to the end of the potential core (referred to as the *hydrodynamic array*). The configuration of the array is similar to that employed by Arndt *et al.* (1997), but we focus on developing algorithms that can identify specific signatures of instability

waves. To minimize contamination of the signal by acoustic waves and pressure fluctuations associated with smaller-scale turbulence, we introduce a *beam-forming* (or *matched-field processing*) technique. The approach is in many ways analogous to aerodynamic noise source identification techniques that have been successfully used in many applications (Gramann & Mocio 1995; Mosher 1996; Piet & Elias 1997; Dougherty & Stoker 1998; Suzuki & Butler 2002; Underbrink 2002; Brooks & Humphreys 2003; Venkatesh, Polak & Narayanan 2003). The idea in these previous studies is to detect the position and amplitude of a noise source that best matches a reference solution (typically a monopole source) in a least-squares sense (cf. Johnson & Dudgeon 1993; Tolstoy 1993; Dougherty 2002). In the present case, we replace the monopole noise source with a spatially evolving eigenfunction obtained from linear stability analysis applied to the measured mean velocity field. Because of limitations on the total number of microphones available, we concentrate on the initial mixing layer (approximately to the end of the potential core) and distribute microphones to target a range of frequencies from $St \ (\equiv f D / U_{jet}) =$ 0.25 to 0.5, which includes the most amplified instability waves. The microphones are also azimuthally distributed to detect instability waves for the axisymmetric and first two azimuthal modes (i.e. $m = 0, \pm 1$ and $\pm 2$).

The remainder of the paper is organized as follows. In the next section, we analyse properties of disturbances associated with a turbulent round jet, review results from linear stability analysis, and describe the proposed beam-forming algorithm. In §3, we outline a preliminary microphone array design based on direct numerical simulation (DNS) of a subsonic round jet by Freund (2001). Subsequently, we describe the experimental facilities, test conditions and final array design for the laboratory-scale jets ($Re \gtrsim 10^5$) based on mean-flow data from particle image velocimetry (PIV) by Bridges & Wernet (2003) and Bridges & Brown (2004) in §4. In §5, we evaluate the capabilities of the proposed technique over a range of Mach numbers ($U_{jet}/a_{\infty} = 0.35$ to 0.90) and temperature ratios ($T_{jet}/T_{\infty} = 0.84$ to 2.70). We also compare the detected instability waves with structures extracted using the proper orthogonal decomposition (POD), as done by Arndt *et al.* (1997). We finally discuss some connections and implications of the results for jet noise and conclude by summarizing the benefits and limitations of the instability-wave detection algorithm.

## 2. Theoretical background and detection algorithm

### 2.1. *Linear hydrodynamic regime*

As illustrated in figure 1, the pressure field of a jet consists of several different disturbances. We here categorize them into three types: (i) linear hydrodynamic disturbances, which we represent by eigenfunctions obtained from linear stability analysis; (ii) nonlinear disturbances, which vorticity and entropy modes associated with turbulence typically generate in the mixing layer; and (iii) acoustic waves. To evaluate each of their contributions to the pressure field, we plot their expected radial decay for the axisymmetric mode ($m = 0$) in figure 2. As an example of a nonlinear disturbance, we consider an inviscid line-vortex ring with a core centred at $r/D = 0.5$, whose pressure field asymptotically decays as $(r - D/2)^{-2}$ in the near field (the decay over the domain of interest is actually close to $\sim (r - D/2)^{-3}$). For an acoustic disturbance, we use a quadrupole (decays as $\sim r^{-3}$ in the near field and $\sim r^{-1}$ in the far field, where $k$ is the axial wavenumber) centred at the jet axis for $St = 0.35$. These disturbances are compared with an eigenfunction of instability waves in the radial direction.
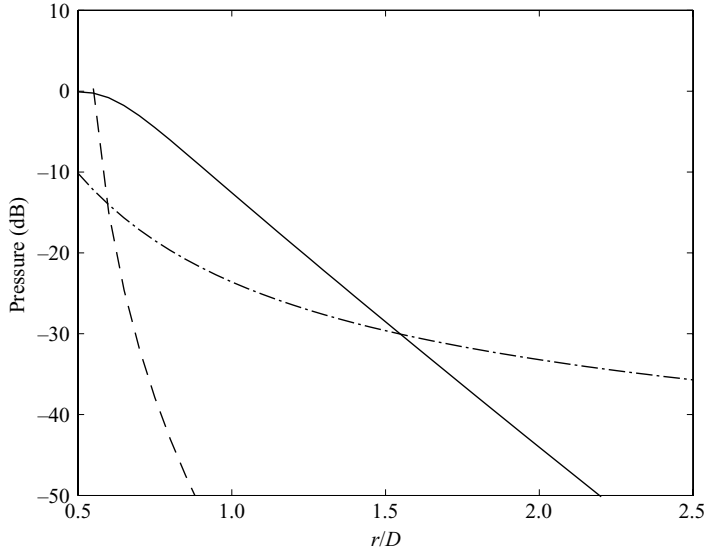
FIGURE 2. Comparison of decay rates in the radial direction: ——, instability waves for $m = 0$ at $St = 0.35$ ($x/D = 2.5$ for case B, shown in table 1); – – –, vortex ring at $r/D = 0.5$; —·—, acoustic quadrupole at the centreline. Magnitudes are arbitrary scaled.

Figure 2 shows that even if the amplitude of the vortex ring is the highest in the mixing layer, its pressure level falls off much faster than that of the instability waves, which decay as $\sim r^{-1/2} \exp[-r\sqrt{k^2 - (\omega/a_\infty)^2}]$, where $\omega$ is the angular frequency. On the other hand, acoustic waves, which decay more gently, can readily dominate the signals at sufficiently large $r$, although their amplitude is typically much smaller than the other two types of disturbance inside the mixing layer. Thus, there exist crossover points, one from nonlinear disturbance to linear hydrodynamic waves and the other from linear hydrodynamic waves to acoustic signals (Crighton & Huerre 1990). The main goal of the hydrodynamic-array design is to identify this 'linear hydrodynamic regime' and distribute microphones in this region to extract signals from instability waves most efficiently.

## 2.2. *Linear stability analysis*

We now briefly review results from linear stability analysis for a weakly non-parallel mean flow. This provides the forms of instability waves, which are later used as reference solutions for the proposed beam-forming algorithm.

We assume that the flow is compressible and inviscid. The ansatz for the instability wave is

$$\Pi(\omega, m, a_s; x, r, \theta) = a_s A(\omega, m; r) e^{-i(\omega t - kx - m\theta)}, \tag{2.1}$$

where $\Pi$ denotes logarithmic pressure (i.e. $\Pi \equiv \gamma^{-1} \log(p/p_\infty)$, $\gamma$ being the specific heat ratio and $p_\infty$ the ambient pressure), $m$ is the azimuthal mode number, and $A$ denotes the eigenfunction, which is arbitrarily normalized here. Note that the eigenfunctions of positive and negative azimuthal modes are identical.

To solve eigenfunctions, we substitute (2.1) into the third-order convective wave operator (Pridmore-Brown 1958; Lilley 1974), which is Fourier-transformed as
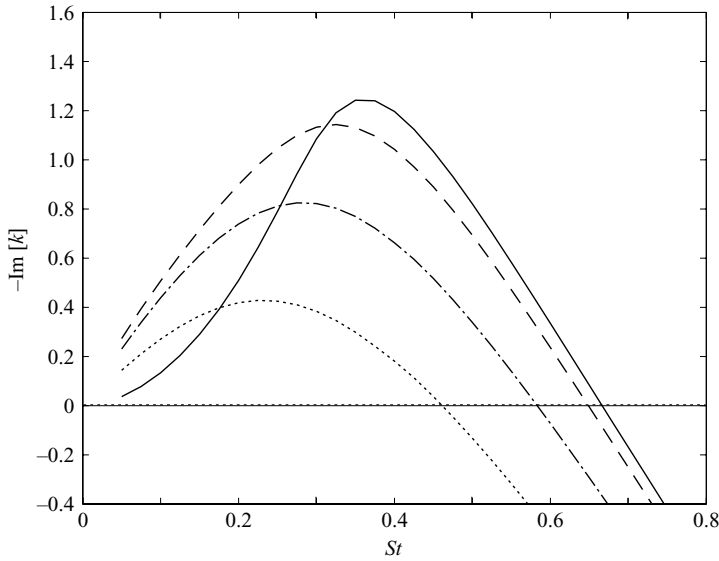
FIGURE 3. Growth rates of instability waves in a round jet ($M_\infty = 0.5$, unheated). A spatial problem is solved based on linear stability analysis, and the imaginary part of the wavenumber is plotted: ——, $m = 0$; – – –, $m = 1$; —·—, $m = 2$; ···, $m = 3$. The mean velocity and temperature profiles were taken from the PIV data (Bridges & Wernet 2003) at $x/D = 2.25$.

follows:

$$\frac{\mathrm{d}}{\mathrm{d}r}\left(\frac{r}{n^2}\frac{\mathrm{d}A}{\mathrm{d}r}\right) + \left(n^2 - k^2 - \frac{m^2}{r^2}\right)\frac{r}{n^2}A = 0, \tag{2.2}$$

where $n(r) \equiv [\omega - kU(r)]/a(r)$, $U(r)$ being the mean velocity in the axial direction (denoted by $x$) and $a(r)$ the mean speed of sound.

The structure of the eigenfunction outside the jet is of special relevance to this study. At a larger radial distance, the Sommerfeld radiation condition must be satisfied:

$$r^{1/2}\left(\frac{\mathrm{d}A}{\mathrm{d}r} - \mathrm{i}\sqrt{n_\infty^2 - k^2}A\right) \to 0 \quad \text{as} \quad r \to \infty, \tag{2.3}$$

where $n_\infty \equiv n(r = \infty)$. At large $r$, the eigenfunction is exponentially decaying when the phase speed is subsonic, i.e. $\omega/k < a_\infty$.

In addition, the asymptotic behaviour of $A(\omega, m; r)$ near the jet axis is given by

$$A(\omega, m; r) \sim r^m \quad \text{as} \quad r \to 0. \tag{2.4}$$

In this study, we are interested in families of the most unstable mode, i.e. the largest $-\mathrm{Im}[k]$, for each $m$. For typical velocity profiles of a subsonic unheated round jet, at most only one family of unstable modes exists for each $m$ (Mattingly & Chang 1974). Figure 3 depicts growth rates of instability waves for the axisymmetric and first two azimuthal modes ($m = 0$ to 2). Each family has a peak growth rate between $St = 0.2$ and 0.4 at a cross-section specified here ($x/D = 2.25$). Since the growth rates of the modes higher than $m = 2$ are much weaker than those of the lower modes, we investigate only up to $m = 2$ in this study.

To take into account the spreading effects of the mixing layer, an eigenfunction is calculated at each axial station, $x$, by assuming that the velocity and temperature profiles are locally parallel. The composite eigenfunction (here in after referred to as
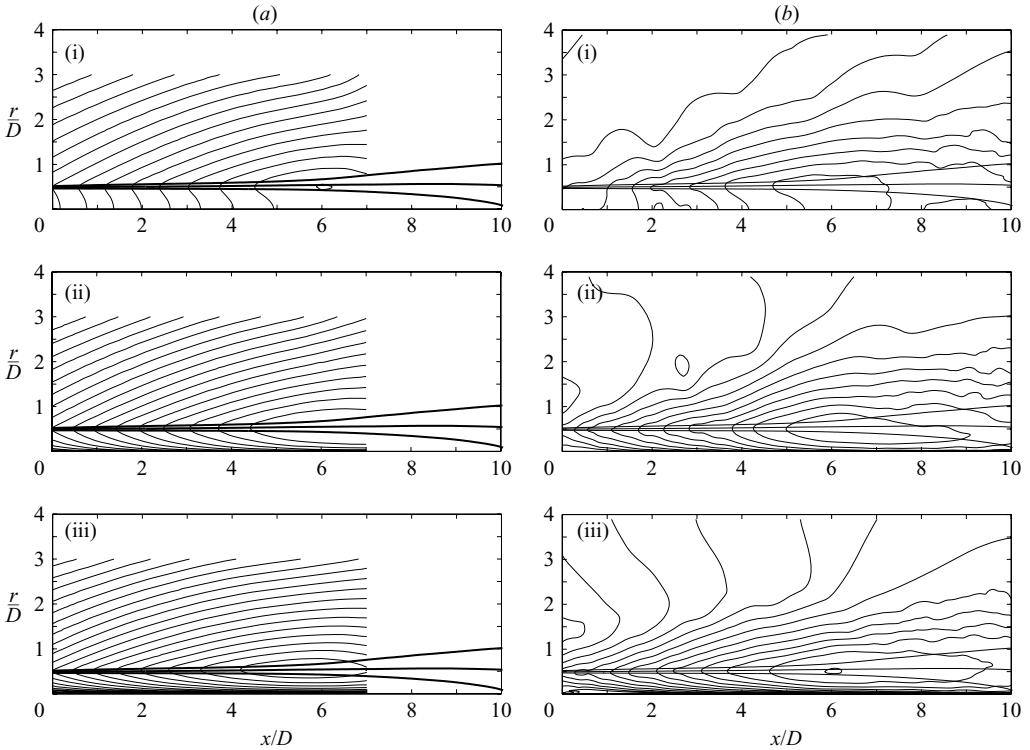
FIGURE 4. (*a*) Pressure contours of eigenfunctions, (2.5), and (*b*) averaged pressure fluctuation
($\sqrt{\overline{|\hat{p}'|^2}}$) from the DNS: (*i*) $m = 0$; (*ii*) $m = 1$; (*iii*) $m = 2$. The contour interval is 6 dB in both
figures. Thicker lines depict iso-mean-velocity contours of $U_{max}/4$, $U_{max}/2$, and $3U_{max}/4$.

the eigenfunction for simplicity) then becomes

$$A(\omega, m; x, r) = \bar{A}(\omega, m; x, r) \exp \left[ i \int_0^x k(\xi) \, d\xi \right], \tag{2.5}$$

where $\bar{A}(\omega, m; x, r)$ is a normalized eigenfunction at each $x$ and $k(\xi)$ is the correspond-
ing complex wavenumber at $x = \xi$. We normalize $\bar{A}$ to be unity (with no imaginary
part) at the radial position where the complex amplitude is maximum.

   In computing the eigenfunctions, the velocity and temperature profiles (either from
DNS or experiment) are fitted with hyperbolic tangent profiles at each cross-section in
a least-squares sense so that the equation can be smoothly integrated. Subsequently,
eigenfunctions are computed by a shooting method with a standard fourth-order
Runge–Kutta scheme. The same scheme is used to integrate the phase part of (2.5).
Special care is taken to circumvent the critical layer (Tam & Morris 1980), where
eigenfunctions decay downstream as the mean flow spreads (see Appendix A for
details).

   Figure 4 compares the magnitude of eigenfunctions (2.5) with the averaged pressure
fluctuations calculated directly from DNS (Freund 2001) at $St = 0.3$. The eigenfunc-
tions capture the exponential growth and successive saturation in the streamwise
direction, especially in $1.75 < x/D < 6.25$. The quantitative agreement is satisfactory
for the $m = 0$ and $m = 1$ modes, while for $m = 2$ the eigenfunction saturates more
rapidly than the result from the DNS. The pressure fluctuations from the DNS
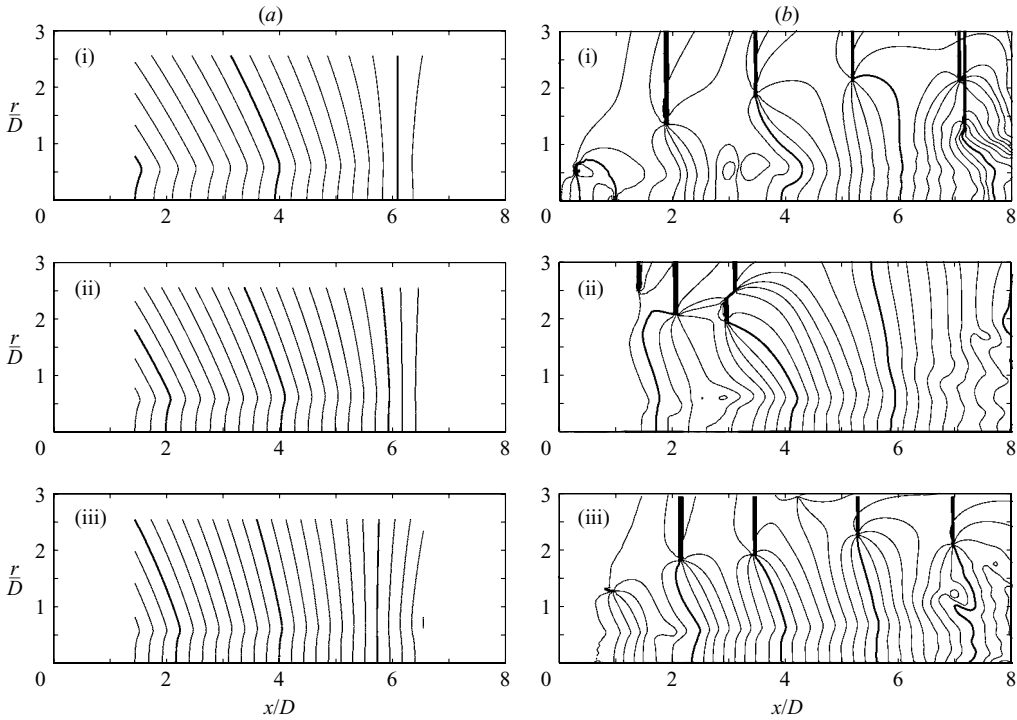
FIGURE 5. (*a*) Iso-phase contours of the eigenfunctions and (*b*) those of the pressure fluctuation from the DNS. Notation is the same as figure 4. The contour interval is 45°, and the thicker lines denote every 360°.

have slower decay at larger radius, where sound-wave amplitude overcomes the hydrodynamic fluctuations, as discussed in the preceding section.

We also compare the phase fields between the eigenfunctions and DNS pressure fluctuations in figure 5. As discussed later, the beam-forming algorithm predicts amplitude based on phase matching. In the phase contours of the DNS, several branch points appear (where multiple contours converge), at which the contribution from acoustic signals exceeds that from instability waves. Therefore, we must place the array closer to the centreline than these points. On the other hand, in the mixing layer we can observe some phase distortion, particularly for $m = 0$ and $m = 1$ near $x/D = 3$, presumably due to nonlinear disturbances. It is also important to notice that the agreement of phase variation in the hydrodynamic region, say $1 < r/D < 2$, is relatively good for the $m = 0$ and $m = 1$ modes, while there is some phase delay in the saturated region ($x/D > 5$) for $m = 2$.

We should remember that the Reynolds number in the DNS is sufficiently low ($Re = 3600$) such that the initial mixing layer is transitional. Compared with the experiments (whose Reynolds numbers are of the order of $Re \gtrsim 10^5$), the DNS flow field has a smaller spreading rate of the mixing layer and a longer potential core. Nonetheless, the wavelengths at our frequencies of interest are nearly the same for both cases. Therefore, the design criteria of a hydrodynamic array assessed with the DNS database are expected to be valid for high-Reynolds-number jets with minimal modifications.

## 2.3. *Beam-forming algorithm*

In this section, we start with the existing beam-forming algorithm (cf. Johnson & Dudgeon 1993; Dougherty 2002) for acoustic source localization. Note that this algorithm is equivalent to the matched field processing (cf. Tolstoy 1993), which has been widely used for underwater acoustics and seismology. Subsequently, we extend it for instability wave identification in the following section.

Suppose sound generated by a monopole source propagates in a free quiescent space. If we take a Fourier transform of pressure (or $\gamma^{-1}\log(p/p_\infty)$, as shown in (2.1)) in time, the pressure fluctuation at the point $\boldsymbol{x}$ may be represented by

$$\hat{p}(\omega, a_s, \boldsymbol{x}_s; \boldsymbol{x}) = \frac{1}{2}\frac{a_s(\omega)}{4\pi|\boldsymbol{x} - \boldsymbol{x}_s|}\mathrm{e}^{\mathrm{i}k|\boldsymbol{x}-\boldsymbol{x}_s|} \equiv a_s\hat{P}(\boldsymbol{x}_s; \boldsymbol{x}), \tag{2.6}$$

where $a_s$ is the complex source amplitude including an arbitrary phase shift. In addition, $k$ denotes the wavenumber, $\boldsymbol{x}_s$ the source position, and $\hat{P}$ the form of a monopole solution in (2.6). We consider $\hat{p}(\omega, a_s, \boldsymbol{x}_s; \boldsymbol{x})$ to be the reference solution for an acoustic source. On the other hand, suppose the pressure data are available at $N_{mic}$ observer points (i.e. microphones) and define the position of the $l$th observer to be $\boldsymbol{x}_l$. At each $\boldsymbol{x}_l$, we Fourier-transform the measured pressure data in time and denote them as $\hat{q}_l(\omega)$. Subsequently, we consider the square norm of the difference between the reference solution and the measured data and define the following cost function:

$$J(\omega, a_s, \boldsymbol{x}_s) \equiv \sum_{l=1}^{N_{mic}} |\hat{p}(\omega, a_s, \boldsymbol{x}_s; \boldsymbol{x}_l) - \hat{q}_l(\omega)|^2. \tag{2.7}$$

Next, we determine the complex source amplitude, $a_s$, that optimizes the cost function above. By differentiating $J$ with respect to $a_s$, the source amplitude that minimizes (2.7) is given by

$$(a_s)_{min}(\omega, \boldsymbol{x}_s) = \frac{\displaystyle\sum_{l=1}^{N_{mic}} \hat{P}^*(\boldsymbol{x}_s; \boldsymbol{x}_l)\hat{q}_l(\omega)}{\displaystyle\sum_{l=1}^{N_{mic}} |\hat{P}(\boldsymbol{x}_s; \boldsymbol{x}_l)|^2}, \tag{2.8}$$

where the superscript $*$ denotes complex conjugation. The quantity, $(a_s)_{min}$, can then be computed at each $\boldsymbol{x}_s$. Substituting (2.8) into (2.7), we obtain the minimized cost function as a function of $\omega$ and $\boldsymbol{x}_s$ as

$$J(\omega, (a_s)_{min}, \boldsymbol{x}_s) = \sum_{l=1}^{N_{mic}} |\hat{q}_l(\omega)|^2 - \frac{\left|\displaystyle\sum_{l=1}^{N_{mic}} \hat{P}^*(\boldsymbol{x}_s; \boldsymbol{x}_l)\hat{q}_l(\omega)\right|^2}{\displaystyle\sum_{l=1}^{N_{mic}} |\hat{P}(\boldsymbol{x}_s; \boldsymbol{x}_l)|^2}. \tag{2.9}$$

Rearranging (2.9) and expressing it in matrix form, we generally generate contours of the following quantity to localize the acoustic source position:

$$Q(\omega, \boldsymbol{x}_s) \equiv |\boldsymbol{q}|^2 - J(\omega, (a_s)_{min}(\omega, \boldsymbol{x}_s), \boldsymbol{x}_s) = \frac{\boldsymbol{P}^\dagger}{|\boldsymbol{P}|}\cdot\boldsymbol{q}\boldsymbol{q}^\dagger\cdot\frac{\boldsymbol{P}}{|\boldsymbol{P}|}, \tag{2.10}$$

where $q \equiv \hat{q}_l(\omega)$, $P \equiv \hat{P}(x_s; x_l)$, and † denotes complex conjugate transpose. The $l \times l$ matrix, $qq^*$, is called the *cross-spectral matrix* and the vector, $P/|P|$ (which has $l$ components), is the *steering vector*. The position where the cost function becomes minimum, and in turn, $Q(\omega, x_s)$ becomes maximum, indicates the source position. At this point, $(a_s)_{min}$ corresponds to the predicted complex source amplitude, and $Q(\omega, x_s)/|P|^2$ to the source intensity. Thus, we can detect the position and amplitude of an acoustic source in a non-contact fashion.

Now, suppose the transformed pressure signals consist of $N_{src}$ ($\leqslant N_{mic}$) uncorrelated noise sources; namely, we expressed them as

$$q \equiv \sum_{l'=1}^{N_{src}} a_{l'} v_{l'}, \tag{2.11}$$

where $a_{l'}$ denotes the complex amplitude of the signals from the $l'$th source and its vector $v_{l'}$ is normalized so that $|v_{l'}| = 1$, but the vectors are not mutually orthogonal in general. If we take an ensemble average of a cross-spectral matrix, the cross-terms between uncorrelated noise sources then vanish. Thus, the averaged cross-spectral matrix can be simplified as

$$\overline{qq^\dagger} = \sum_{l'=1}^{N_{src}} \overline{|a_{l'}|^2} v_{l'} v_{l'}^\dagger. \tag{2.12}$$

On the other hand, the cross-spectral matrix can be diagonalized with a unitary matrix because it is Hermitian. Therefore, the following relation holds:

$$\sum_{l=1}^{N_{mic}} \lambda_l u_l u_l^\dagger = \sum_{l'=1}^{N_{src}} \overline{|a_{l'}|^2} v_{l'} v_{l'}^\dagger \quad \text{or} \quad \lambda_l = \sum_{l'=1}^{N_{src}} \overline{|a_{l'}|^2} |u_l^\dagger \cdot v_{l'}|^2, \tag{2.13}$$

where $\lambda_l$ is the $l$th eigenvalue (non-negative) and $u_l$ is the corresponding orthonormal eigenvector (i.e. $|u_l| = 1$ and orthogonal to each other). The set of eigenvectors is equivalent to the POD modes in the frequency space (Arndt *et al.* 1997). This equation shows that when the primary signal has by far the greatest amplitude, the square root of the first eigenvalue, i.e. $\sqrt{\lambda_1}$, approximately gives the amplitude of this signal, and its eigenvector, $u_1$, coincides with the normalized signal, $v_1$. Thus, the POD is useful particularly when we extract distinctive signals without knowing their information *a priori*. However, if amplitudes of multiple signals are comparable, each eigenvector does not coincides with an individual uncorrelated signal in general. Moreover, as the mode number, $l$, increases on the left-hand side of (2.13), the subspaces occupied by the preceding eigenvectors (i.e. $< l$) prevent spanning dimensions from capturing the correlated signals. Thus, eigenvectors of a cross-spectral matrix do not necessarily separate uncorrelated signals nor extract correlated signals, while the beam-forming can detect the amplitude projected onto the reference solution.

## 2.4. *Detection of instability waves*

We extend the discussion above to the detection of instability waves. We similarly assume that the pressure histories are available at $N_{mic}$ observer points (which are distributed just outside of the mixing layer) and define the transformed logarithmic pressure at the $l$th observer to be

$$\hat{\Theta}_l(\omega) \equiv \frac{1}{2\pi} \int_0^\infty \frac{1}{\gamma} \log \left[ \frac{p(t, x_l, r_l, \theta_l)}{p_\infty} \right] e^{i\omega t} \, dt. \tag{2.14}$$

We also transform the eigenfunction (2.1), which is computed with given $U(r)$ and $a(r)$, and define it as $\hat{\Pi}(\omega, m, a_s; x_l, r_l, \theta_l)$. Subsequently, we introduce a cost function as

$$J(\omega, m, a_s) \equiv \sum_{l=1}^{N_{mic}} |\hat{\Pi}(\omega, m, a_s; x_l, r_l, \theta_l) - \hat{\Theta}_l(\omega)|^2. \tag{2.15}$$

From (2.8), the amplitude of the instability waves is then estimated as

$$(a_s)_{min}(\omega, m) = \frac{\displaystyle\sum_{l=1}^{N_{mic}} A^*(\omega, m; r_l) \exp(-\mathrm{Im}[k]x_l) \exp(-\mathrm{i}(Re[k]x_l + m\theta_l))\hat{\Theta}_l(\omega)}{\displaystyle\sum_{l=1}^{N_{mic}} |A(\omega, m; r_l)|^2 \exp(-2\mathrm{Im}[k]x_l)}, \tag{2.16}$$

for each $\omega$ and $m$. Thus, the magnitude of instability waves, $|(a_s)_{min}|$, and its phase, $\arg[(a_s)_{min}]$, for each $m$ at a given $\omega$ can be computed from pressure time histories at $N_{mic}$ observer points. To be precise, the eigenfunctions are also functions of $x$ in this study, since we take into account the mean flow variation in the axial direction (refer to (2.5)).

It should be mentioned that the principal idea of the beam-forming is detection based on phase matching. As seen from (2.10), the quantity $Q(\omega, x_s)$ is nearly maximized when the phases of the steering vector best match those of the cross-spectral matrix. From the DNS data, the agreement in figure 5 demonstrates the feasibility of prediction based on phase matching, while the agreement in figure 4 strongly indicates that the reference solution represents a large-scale coherent structure over a substantial region of a jet. Because the amplitude acts as a weight function, phase is most closely matched where the amplitude is highest. In detection of acoustic sources, variation in amplitude is generally insignificant provided that the array is reasonably far from the source, relative to the aperture. By contrast, signals from instability waves exponentially grow in the axial direction; therefore, we must carefully distribute observer points so that amplitude variation between them is sufficiently small. This, in turn, helps reduce uncorrelated noise between microphones.

## 3. Array design guidelines from DNS

To develop design procedures of the hydrodynamic array and evaluate the potential accuracy of the proposed detection method, the DNS database computed by Freund (2001) for a round jet at a Mach number of $M_{jet} \equiv U_{jet}/a_{jet} = 0.9$ and a Reynolds number of $Re \equiv U_{jet}D/\nu = 3600$ was used. Figures 1, 4 and 5 were generated from this database. The details of numerical procedures may be found in Freund (2001).

Using the mean flow field from the DNS database, we construct reference solutions for $St = 0.3$ following the procedures described in §2.2. We calculate the amplitude of instability waves for each azimuthal mode with the proposed beam-forming algorithm using every other grid point in the region indicated in figure 6, and treat this as the exact amplitude. Subsequently, we try to recover this amplitude from a limited number of microphones and evaluate the accuracy as a function of a microphone number and their distribution.

The overall results based on the DNS suggest that the array requires at least seven rings in the streamwise direction and each ring requires six microphones (i.e. a total of 42 microphones) to resolve modes up to the $m = 2$. The azimuthal angles of the
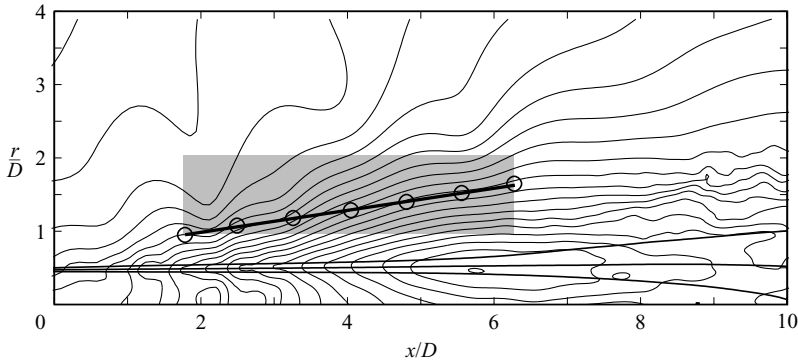
FIGURE 6. The domain where the amplitude of the reference solutions is calculated (denoted by a grey region), and the line along which the microphones are distributed (denoted by a solid line) in the DNS test. As an example, seven microphones (i.e. rings) are distributed along the line. Contours of pressure fluctuations over $m = -9 \sim 9$ are superposed with an interval of 3 dB.

microphones are staggered in every other ring (i.e. 30°, 90°, 150°, 210°, 270° and 330° for the first ring; 0°, 60°, 120°, 180°, 240° and 300° for the second ring, and so on) in order to suppress aliasing errors from higher azimuthal modes. The axial length of the array is set to cover two wavelengths of the instability waves, and the spreading angle of the array is determined so that the variation of pressure intensity is within the same order of magnitude (8.7° in the DNS). The position of the array used with the DNS database is displayed in figure 6. The accuracy of detection using this model array is estimated to be of the order of 10 % ($\sim$ 1 dB) for $m = 0$ and 30 % ($\sim$ 3 dB) for $m = 1$ and 2 in pressure amplitude, respectively. Since the reference domain is determined by referring to the $m = 0$ mode, the errors in the other two modes appear to be larger in the DNS.

## 4. Experimental facilities and data processing

### 4.1. *Small hot jet acoustic rig*

Experiments were conducted using the small hot jet acoustic rig (SHJAR) at NASA Glenn Research Centre. A single-stream round jet was mounted 3.05 m from the ground in an anechoic dome with a 20 m radius. The wall of the dome was filled with foam wedges. The jet exit was a converging nozzle, and the exit diameter was 5.08 cm (2.0 in). We tested a variety of combinations of Mach numbers ($M_\infty \equiv U_{jet}/a_\infty = 0.35$ to 0.90) and temperature ratios ($T_{jet}/T_\infty = 0.84$ to 2.70). These conditions followed the set points of the previous experiment by Tanna (1977). Bridges & Wernet (2003) and Bridges & Brown (2004) summarized the flow characteristics in most of these cases. Table 1 shows the flow conditions considered in this study. Note that velocity fluctuation from the designated test conditions was within 1 %.

### 4.2. *Mean flow data from PIV*

To construct the eigenfunctions for the experimental cases, we used mean flow data measured by Bridges & Wernet (2003) and Bridges & Brown (2004). Velocity fields on cross-sectional and streamwise planes were obtained using PIV with resolutions of approximately $0.1D$ and $0.02D$ in the streamwise and the radial directions, respectively. Although the mean flow fields for cases A, C and G were not available,

| Case | Set point | $M_\infty$ ($M_{jet}$) | $T_{jet}/T_\infty$ | $Re$ | PIV flow data availability |
|------|-----------|------------------------|---------------------|------|----------------------------|
| A | 1 | 0.35 (0.35) | 0.98 (cold) | $4 \times 10^5$ | No |
| B | 3 | 0.50 (0.51) | 0.96 (cold) | $7 \times 10^5$ | Yes |
| C | 5 | 0.70 (0.74) | 0.91 (cold) | $11 \times 10^5$ | No |
| D | 7 | 0.90 (0.98) | 0.84 (cold) | $16 \times 10^5$ | Yes |
| E | 23 | 0.50 (0.38) | 1.76 (hot) | $2 \times 10^5$ | Yes |
| F | 27 | 0.90 (0.69) | 1.76 (hot) | $4 \times 10^5$ | Yes |
| G | 42 | 0.50 (0.31) | 2.70 (hot) | $1 \times 10^5$ | No |
| H | 46 | 0.90 (0.56) | 2.70 (hot) | $2 \times 10^5$ | Yes |

TABLE 1. Operating conditions of jet flows. $M_{jet} \equiv (U/a)_{jet}$ and $Re \equiv (\rho U D/\mu)_{jet}$.
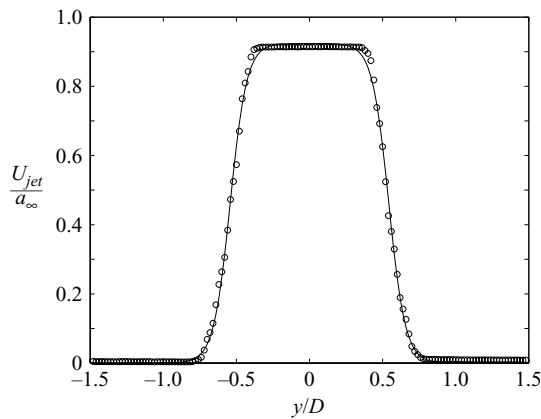


FIGURE 7. Velocity profile at $x/D = 2$ (case D): $\circ$, data from the PIV; ———, approximate hyperbolic-tangent profile used for the linear stability analysis.

they were estimated from case B, the average of cases B and D, and case H, respectively, by scaling with the free-stream jet velocity ignoring compressibility.

To integrate (2.2) smoothly, we fitted the axial mean-velocity data with a hyperbolic tangent profile, $U_0(r) \approx U_{max}/2(\tanh[s(r+r_0)] - \tanh[s(r-r_0)])$. These three parameters, $U_{max}$, $s$ and $r_0$, were optimized in a least-squares sense at each cross-section (see figure 7). From the axial velocity profiles, temperature profiles were estimated using the Crocco–Busemann relation. The agreement with data obtained from total pressure and temperature probes for the case with the highest temperature ratio (case H) is shown in figure 8.

### 4.3. *Hydrodynamic array*

Starting with the overall requirements for the array design obtained from the DNS analyses in §3, we modified the design to account for diffusiveness of the mean velocity profiles in the experiments. In particular, the Reynolds numbers under the laboratory conditions are one to two orders of magnitude higher than that of the DNS. Hence, the mixing layer of the jet spreads more rapidly, and the potential core becomes shorter.

To determine the size of the array in the axial direction, we calculated instability wavelengths at several frequencies for $m = 0$, 1 and 2 based on the PIV mean flow (see
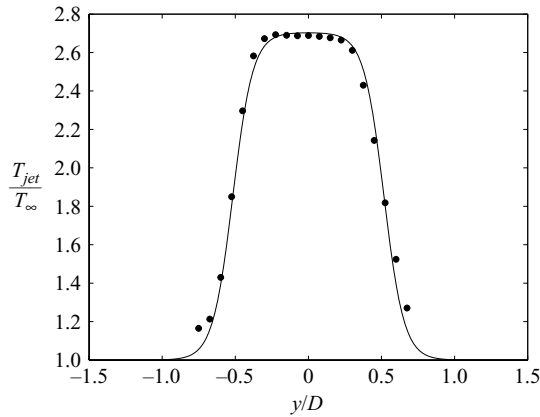
FIGURE 8. Temperature profile at $x/D = 2$ (case H): ●, data from direct probe measurement; ——, approximate profile computed from the velocity profile using the Crocco–Busemann relation.

| | $m = 0$ | $m = 1$ | $m = 2$ |
|---|---|---|---|
| $St = 0.25$ | 3.30 | 2.47 | 2.13 |
| $St = 0.30$ | 2.47 | 1.97 | 1.75 |
| $St = 0.35$ | 1.87 | 1.63 | 1.49 |
| $St = 0.50$ | 1.17 | 1.13 | 1.09 |

TABLE 2. Wavelengths of instability waves (relative to the jet diameter) obtained from the experimental velocity and temperature profiles for case B at $x/D = 2.25$.

table 2). We chose an unheated jet at $M_\infty = 0.5$ (case B) as the base-line case for the design and used the mean velocity and temperature profiles at $x/D = 2.25$, which is, in turn, approximately the centre of the array in the axial direction. Table 2 indicates that the array must extend to $5D$ in order to cover two wavelengths of these modes at $St = 0.3$ (see $m = 0$ in table 2). Hence, even if the array starts at $x/D = 0$, it would nearly reach the end of the potential core, beyond which the assumption of the locally parallel mean flow fails. On the other hand, we cannot locate microphones very close to $x/D = 0$ because of possible interference near the nozzle exit. In particular, some modes associated with internal aerodynamics were observed in unheated jets at higher Mach numbers (refer to Appendix B). As a compromise, we set the array length to be $3.75D$, starting approximately at $x/D = 0.35$.

The spreading angle of the array (the half-angle of the cone) was set to be $11.3°$. This angle was determined so that it was slightly steeper than the spreading angle of the PIV velocity fluctuation. To test various radial positions of microphones, additional rings were introduced with equal spacings (the total number of the rings is 13). Hence, by shifting the whole array in the axial direction by an increment of the ring spacing and by choosing a different set of seven rings, pressure signals can be measured at different radial distances. The radius at the centre of the array was then varied in the range of $1.0 \leqslant r/D \leqslant 1.75$ (at $x/D = 2.25$). The resulting configuration of the hydrodynamic array for the experiments is illustrated in figure 9. Note that
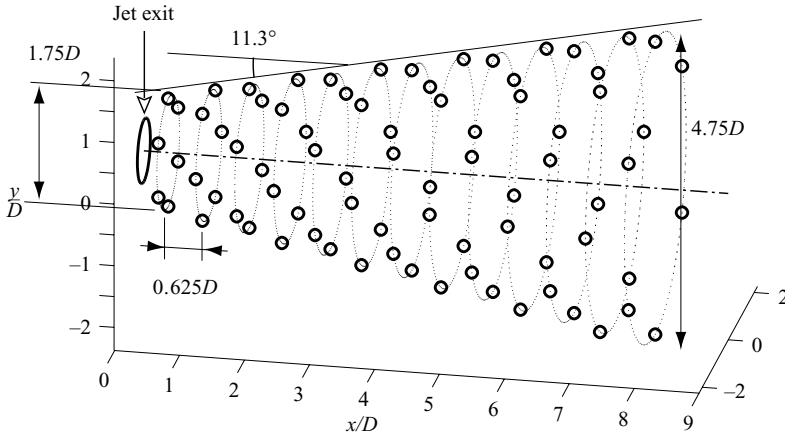
FIGURE 9. Microphone distribution of the hydrodynamic array designed for the experiments.
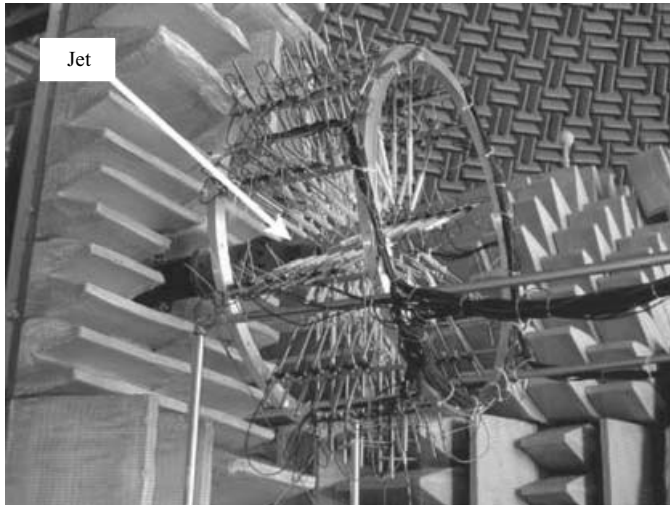


FIGURE 10. Photograph of the hydrodynamic array with the SHJAR facility.

when the array was shifted upstream to measure pressure signals at a larger radius, the first few upstream rings were removed.

The overall microphone array consisted of 13 ring with 6 microphones each, for a total of 78 quarter-inch microphones (note that Arndt *et al.* (1997) used 8 unequally spaced rings with 4 microphones per ring and took the data along 10° and 15° from the centre of the jet exit). Each microphone was supported by a non-conductive plastic sleeve, and it was joined to a stinger mounted on a cylindrical steel frame with 1.22 m diameter and 0.42 m axial length. The whole array was mounted on a structure with wheels to adjust the axial position (figure 10). The error in microphone position was estimated to be less than $0.05D$ based on a noise-source test using a spark plug. This error was at most 5 % of the instability wavelength (table 2). The background noise amplitude was at least three orders of magnitude smaller than signals from the jet.

## 4.4. *Data acquisition and uncertainty in data processing*

We set a sampling rate of 50 kHz and low-pass-filtered pressure signals to 20 kHz; thus, for example, the frequency resolution is approximately up to $St = 3$ at $M_\infty = 0.9$ for an unheated jet. In computing Fourier transforms in time, four period segments at each target frequency were processed (approximately corresponding to 1/6 octave bandwidth). Although no windowing function was applied to the segments, the uncertainty in amplitude of instability waves due to windowing is estimated to be less than 3 % ($\sim$0.25 dB). For each flow condition, pressure histories were recored for 10 s so that at least 500 four-period segments at the target frequency can be processed. If the number of intervals is decreased from 500 to 250, possible variation in amplitude of instability waves is less than 5 % ($\sim$0.4 dB). To plot the amplitude of pressure based on Fourier transforms and beam-forming, the root mean square was taken over 500 segments.

We also consider the aliasing error from higher azimuthal modes. Since the pressure disturbances from fine-scale turbulence generally decay rapidly with radius, the largest contamination is most probably due to coherent structures (i.e. instability waves for $m = 4, 5, 6$, etc.). In particular, the contamination of the $m = 2$ mode by $m = 4$ is considered the greatest because growth rates are decreased with increasing azimuthal mode number. To evaluate this uncertainty, we carried out the following test. We constructed the eigenfunction of $m = 4$ for case B with the amplitude normalized to unity at $(x/D, r/D) = (0.0, 0.5)$ and applied the beam-forming algorithm to this signal with the reference solution for $m = 2$; as a result, we obtained an amplitude of 0.148 (if we apply this to the eigenfunction for $m = 2$, we recover an amplitude of unity). Assuming that the disturbance level of instability waves at the exit for $m = 4$ is equal to that for $m = 2$ (which can be confirmed in figure 16 later), the contamination from $m = 4$ in $m = 2$ is less than 1.2 dB even if they are perfectly correlated and 0.1 dB if uncorrelated.

As mentioned before, we observed strong signals that are not associated with instability waves near the nozzle exit in unheated jets at higher Mach numbers (see Appendix B). This causes an increased pressure amplitude at the first ring up to 10 Pa at $St = 0.35$ for case D, for example (this effect can be seen in figure 18*a*). However, by applying the beam-forming algorithm, we can mostly eliminate this influence. The estimated increase in instability-wave amplitude is of the order of 0.1 % even if this signal is perfectly correlated with instability waves. This ensures that the amplitude at the exit can be appropriately determined even when the influence of this signal varies in a range of Mach numbers (refer to figure 16).

## 5. Results and discussion

### 5.1. *Capabilities of the measurement technique*

To evaluate the capabilities of the proposed detection algorithm, we compare the eigenfunctions whose amplitudes are determined by the beam-forming algorithm to pressure fluctuations processed with either Fourier transforms or the POD. In this section, we consider the radial decay, streamwise evolution and phase correlation of the instability waves. The comparisons reveal the extent to which the actual pressure field is composed of linear instability waves, and help identify possible causes for discrepancies where they exist. We choose case B ($M_\infty = 0.5$, unheated) for reference throughout this section unless otherwise noted. In what follows, we refer to the data that are Fourier-transformed in time and the azimuthal direction at each ring
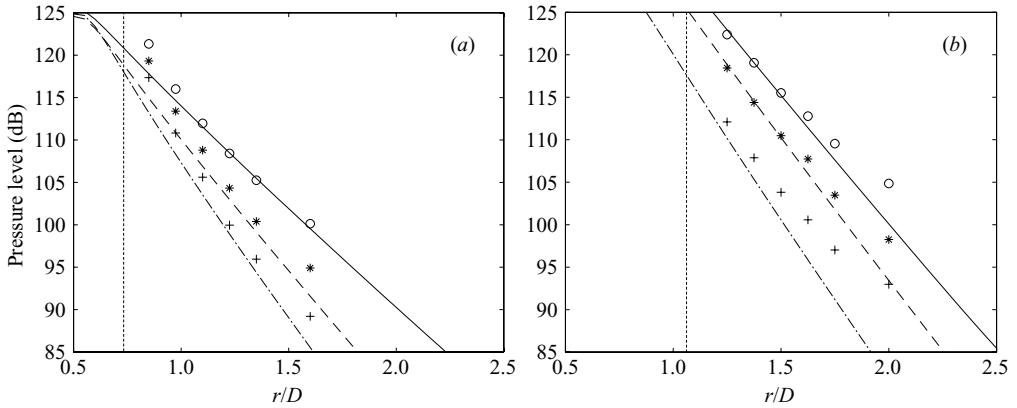
FIGURE 11. Pressure levels of two different cross-sections at several radial microphone positions (at $St = 0.35$ in case B). Pressure levels detected using the beam-forming (i.e. eigenfunction): ——, $m = 0$; — — —, $m = 1$; — · —, $m = 2$. Ring-wise pressure amplitude: ○, $m = 0$; *, $m = 1$; +, $m = 2$. Values are obtained by interpolation at the cross-section of (*a*) $x/D = 1.5$; (*b*) $x/D = 3.5$. The radius of 1 % $U_{jet}$ in the mean velocity is denoted by a vertical dashed line.

as the *ring-wise* pressure amplitude in order to distinguish them from point-wise measurements or axially non-local quantities, such as detected instability waves or POD modes.

We begin by considering the radial decay of pressure. As mentioned in § 4.3, to obtain independent data sets at different radii, we shifted the array to six axial positions for a given flow condition. Figure 11 plots ring-wise pressure amplitude and the eigenfunctions whose magnitudes are given from the beam-forming at two cross-sections. Although the negative azimuthal modes (i.e. $m = -1$ and $-2$) are not plotted here, their amplitudes are statistically identical to the corresponding positive modes. The target frequency is chosen to be $St = 0.35$, which is close to the most amplified frequency of hydrodynamic fluctuations for $m = 0$ (note that the frequency of peak sound radiation in the far field is close to $St \approx 0.2$). At both cross-sections, there is a substantial region of exponential decay, for which the amplitude is detected to within the 1 dB uncertainty. The largest discrepancy is found for $m = 2$, and this is probably from the aliasing error discussed in § 4.4.

Near the nozzle exit ($x/D = 1.5$), the ring-wise data deviate above the eigenfunctions for small $r$. As discussed in § 2.1, nonlinear interactions in the mixing layer can create strong pressure deficits which decay faster than the instability waves. Farther downstream ($x/D = 3.5$), we observe an expected crossover between exponential decay (instability wave) and algebraic decay (acoustic wave) at large $r$. These results suggest that the third or fourth microphone array position can extract the signals from linear hydrodynamic waves most effectively. We performed the same tests for all other cases discussed in this paper and found similar results. Moreover, the amplitude variation among axial microphone positions for these two configurations is within the same order of magnitude in most cases. Therefore, for the rest of the study, we choose the third microphone position from the centre, unless otherwise noted.

Next, streamwise evolution of instability waves is shown in figures 12(*a*)(i)–(iii) at $St = 0.25$, 0.35, and 0.50, respectively. To be precise, the evolution is plotted along the conical array; hence, the signals appear to saturate and decay more rapidly than they evolve in the axial direction at a constant $r$. At a lower frequency ($St = 0.25$),
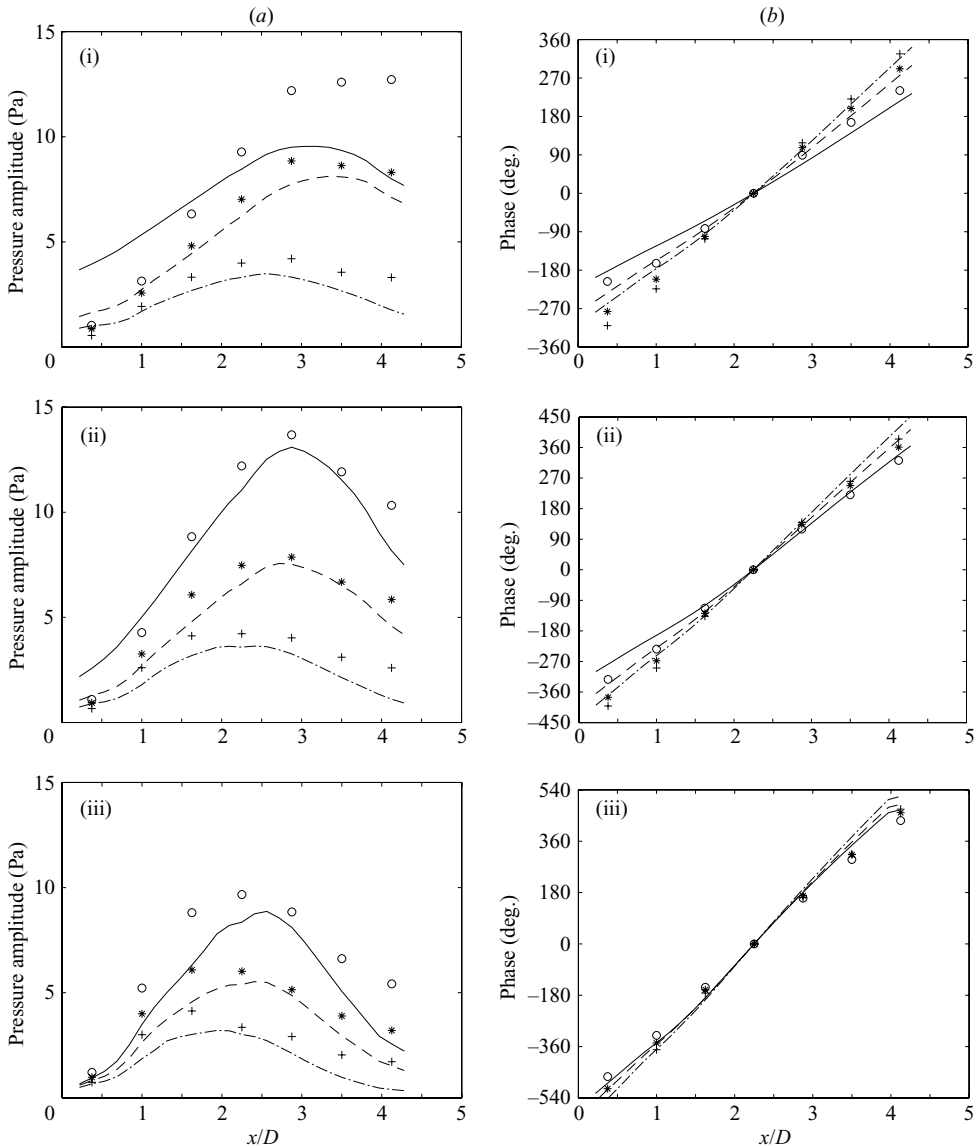
FIGURE 12. (*a*) Evolution of pressure amplitude along the microphone array (ring-wise pressure amplitudes are compared with the eigenfunctions), and (*b*) averaged phase correlation along the microphone array (phase shifts of the eigenvector of the cross-spectral matrix are compared with those of the eigenfunctions) (case B): (i) $St = 0.25$; (ii) $St = 0.35$; (iii) $St = 0.50$. Notation is the same as figure 11.

the ring-wise measurements for the $m = 0$ mode grow faster near the nozzle exit compared with the eigenfunction, while those for $m = 1$ and $m = 2$ closely follow the eigenfunctions. As the frequency is increased ($St = 0.35$), the discrepancy in $m = 0$ is much improved, while the agreement at the higher azimuthal modes is only slightly worse. At a still higher frequency ($St = 0.50$), the growth rates of all three modes are somewhat under-predicted, although the overall evolution, i.e. growth – saturation – decay, is captured well.

It should be mentioned that since the beam-forming algorithm attempts to eliminate signals other than the target instability mode, the estimated amplitude of instability waves is generally lower than the pressure level obtained from Fourier transforms. It is possible to minimize, for example, contributions from convecting turbulence at the same frequency but uncorrelated from instability waves, as shown in (2.12). Moreover, an aliasing error arises from the higher azimuthal modes, and its signal to noise ratio is different between these three modes. The pressure level in $m = 2$ includes the $m = 4$ mode, whose relative intensity is higher than that of the contamination in $m = 0$ (from $m = 6$) and $m = 1$ (from $m = 5$). As mentioned in §4.4, the amplitude given by the beam-forming can contain the aliasing error up to 15 % for $m = 2$, if perfectly correlated. Nonetheless, the proposed algorithm captures streamwise evolution well, except for the axisymmetric mode at low frequencies.

We should emphasize that linear stability analysis predicts the growth rate of $m = 0$ to be much lower than that of $m = 1$ at frequencies lower than the peak (see figure 3). In an axisymmetric jet, the length scale that governs the eigenfunction for $m = 0$ is the jet diameter at low frequencies, while that for the higher azimuthal modes is the vorticity thickness of the shear layer over a wider frequency range (the former mode is analogous to the mode sometimes referred to as a *preferred mode*, and the latter as a *shear-layer mode*, cf. Petersen & Samet 1988). Based on the PIV mean flow data for case B, we find only a single unstable mode, which is associated with the diameter at the nozzle exit (in contrast, we find two modes in case H at $St \gtrsim 0.55$, for example). This difference originates from the centreline condition of the eigenvalue problem; namely, $\partial p'/\partial r = 0$ for $m = 0$ and $p' = 0$ for others. In the actual ring-wise data, however, the growth rates at $St = 0.25$ and $St = 0.35$ are comparable as shown in figure 12($a$); as a result, the discrepancy in $m = 0$ at the lowest frequency is by far the greatest. This point is further discussed at the end of the section.

Phase correlation among the rings in the streamwise direction is shown in figure 12($b$). To obtain the phase correlation, the time histories of pressure data are Fourier-transformed in time and the azimuthal direction, and a cross-spectral matrix of the seven rings ($7 \times 7$) is generated; subsequently, the phase-shift of the eigenvector with the greatest eigenvalue of the cross-spectral matrix is plotted relative to the fourth ring, and this is compared with the phase relation of the eigenfunction in each azimuthal mode. This method can eliminate the signals from acoustic waves near the end of the potential core and those propagating upstream near the nozzle, as discussed in next section (on the other hand, this method is not preferable for the previous two tests because, as we show later, the eigenvectors capture the amplitude evolution only near the saturated region).

In general, the agreement is fairly good in all cases. Although the disturbance level that is not associated with large-scale structures may be higher in the experiments than that in the DNS, the agreement over a sufficient axial extent guarantees the beam-forming algorithm to work. To be precise, at $St = 0.25$ in figure 12($b$)(i), the phase correlations in all three modes indicate that the length scales of the hydrodynamic structures are slightly shorter than those predicted from the linear stability analysis. In contrast, the actual phase shifts are slower than the prediction at $St = 0.50$ in all modes. Similar to the streamwise evolution, the overall agreement is the best at the middle frequency ($St = 0.35$). These results are unchanged even if we narrow the frequency response by increasing the sampling time segment from 4 to 16 periods. We observe that the signals in the experiments tend to deviate in the direction toward the most amplified frequency of the near field, although the degree of deviation is sufficiently small (of the order of $10°$) for the beam-forming to work.
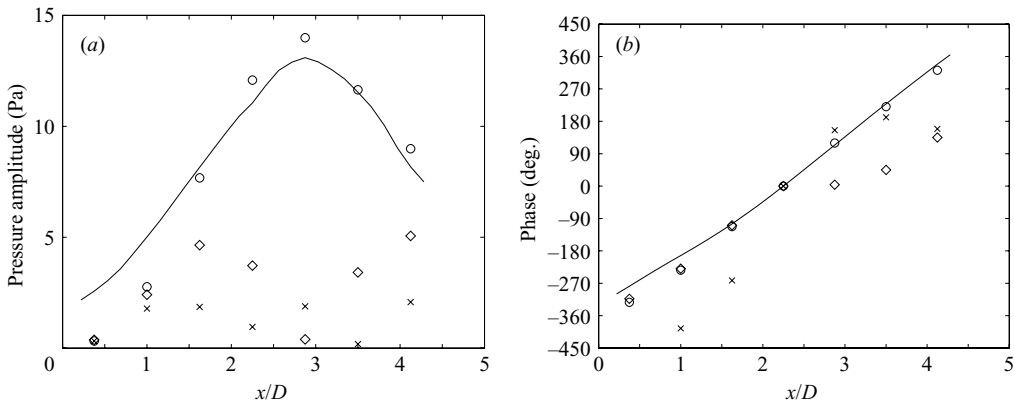
FIGURE 13. Comparison between the first three eigenvectors of the cross-spectral matrix and the eigenfunction based on the linear stability analysis ($m = 0$ at $St = 0.35$ for case B): $\bigcirc$, eigenvector with the greatest eigenvalue; $\diamond$, that with the second; $\times$, that with the third; ——, eigenfunction. (*a*) amplitude; (*b*) phase correlation.

The results of both amplitude evolution and phase correlation consistently show that the frequency that can be most accurately captured by the beam-forming is the most amplified frequency. To be precise, the most unstable frequency decreases slightly with increasing azimuthal mode number. The trends of deviation at both lower and higher frequencies indicate that the signals are contaminated from the most amplified modes. It has been also reported in experiments (Mankbadi 1985) as well as simulations (Mohseni, Colonius & Freund 2002) that the growth rates at off-peak frequencies tend to be under-predicted by the linear stability analysis. The current results show that the discrepancy becomes particularly noticeable near the nozzle exit for $m = 0$ at low frequencies.

In theory, since an eigenfunction is a discrete solution for a given frequency, the phase relation and the growth rate should be uniquely determined for each $m$. We should remember, however, that the eigenfunctions in this study are constructed assuming that the flow is locally parallel. At low frequencies, the instability wavelength becomes comparable to the length of the potential core (see table 2). Therefore, the assumption of locally parallel flow is probably no longer valid, and this may cause significant discrepancy near the nozzle exit. To calculate the growth rates accurately, we must expand the equation including the spreading rate of the mixing layer in linear stability analysis (Crighton & Gaster 1976; Tam & Morris 1980).

### 5.2. *Eigenvectors of the cross-spectral matrix*

To further investigate the signals from the hydrodynamic array, we study eigenvectors of cross-spectral matrices (i.e. POD modes). In fact, several previous studies have analysed coherent structures in the jet mixing layer based on the POD technique (Arndt *et al.* 1997; Bonnet *et al.* 1998; Citriniti & George 2000). Here, we process $7 \times 7$ cross-spectral matrices in the same way as described for the phase correlation above. Figure 13 plots the first three eigenvectors for $m = 0$ (eigenvectors multiplied by the square root of the corresponding eigenvalues in figure 13(*a*) and their phase correlation in figure 13(*b*)). The first eigenvector (i.e. the one with the greatest eigenvalue) approximately follows the evolution of instability waves; however, the mode shape of the eigenvector deviates substantially from the eigenfunction near the nozzle exit. The
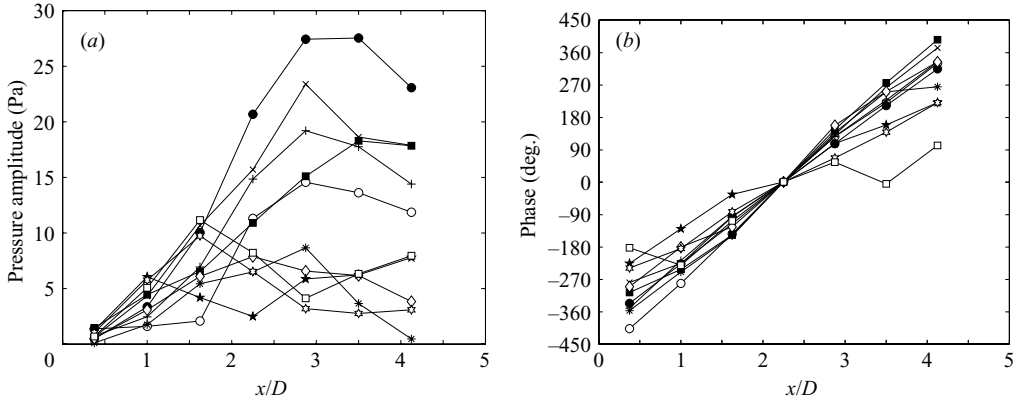
FIGURE 14. Ring-wise pressure of ten samples for $m = 0$ at $St = 0.35$ (case B): (*a*) amplitude; (*b*) phase. Four periods of the target frequency were Fourier-transformed. Each symbol corresponds to one sample.

second eigenvector depicts the same behaviour upstream, but does not capture the amplitude near the saturated region. The phase correlation confirms the agreement of the first eigenvector with the prediction based on the linear stability analysis.

We should emphasize that during each sampling period, instability waves only partially occupy the domain of interest in the form predicted by linear stability analysis. Figure 14 depicts ring-wise pressure amplitude and the phase correlation of the first ten sampling segments for $m = 0$. Some samples follow the initial growth, and others capture the saturated region in amplitude. The characteristic length of the occupancy, i.e. the correlated length scale, is typically shorter than the length of the array. As a result, the first eigenvector represents only the mode-shape near the peak amplitude, where the 'energy' is concentrated, and rapidly decays upstream and downstream (see figure 13*a*). Consequently, the second and even third eigenvectors capture the instability waves upstream, but do not capture the peak amplification in the streamwise direction. Recall that from (2.13), each eigenvector must be orthogonal to the preceding ones. Thus, a single POD mode does not always represent an instability-wave component in amplitude. On the other hand, phase deviation caused by uncorrelated signals is cancelled when the cross-spectral matrices are averaged over many segments; hence, excellent agreement between the phase correlation of the first eigenvector and the linear stability analysis is obtained, as seen in figure 13(*b*).

At a higher Mach number ($M_\infty = 0.9$), the trend explained above can be observed more clearly. Amplitude and phase of the first three eigenvectors are plotted in figure 15. Although the growth rate of the instability wave is estimated well, the down-stream decay is not captured by the first eigenvector. As discussed in the next section, the downstream plateau indicates that the signals are contaminated by acoustic waves (most probably associated with instability waves). Since these acoustic signals are correlated with instability waves, the first eigenvector is composed of both instability and acoustic waves and its magnitude cannot be accurately determined by the square root of the eigenvalue.

The phase correlation of the second eigenvector in figure 15(*b*) indicates an upstream-propagating mode. This wave is a neutral acoustic mode decaying in the radial direction (i.e. a discrete solution), and the wavenumber calculated based on the convective wave operator (2.2) actually predicts its phase evolution near the nozzle
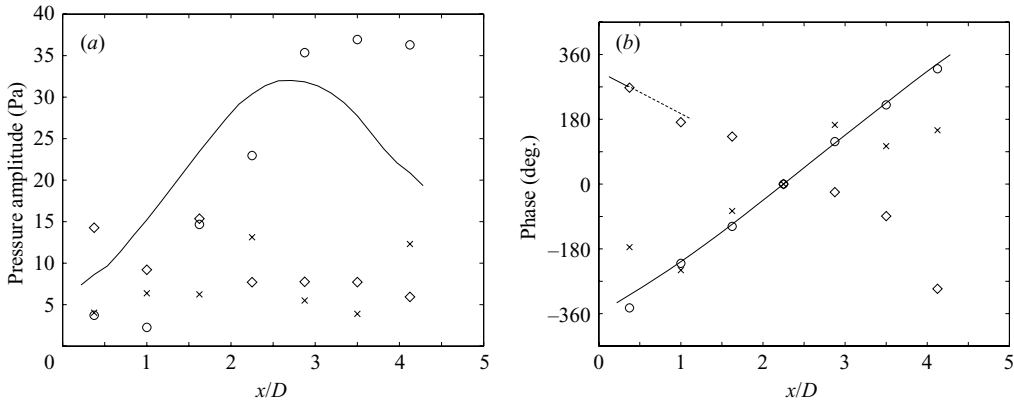
FIGURE 15. Comparison between the first three eigenvectors of the cross-spectral matrix and the eigenfunctions based on the linear stability analysis at $M_\infty = 0.9$ ($m = 0$ at $St = 0.35$ for case D). Notation is the same as figure 13. The dashed line in (*b*) denotes phase evolution of an up-propagating neutral acoustic mode.
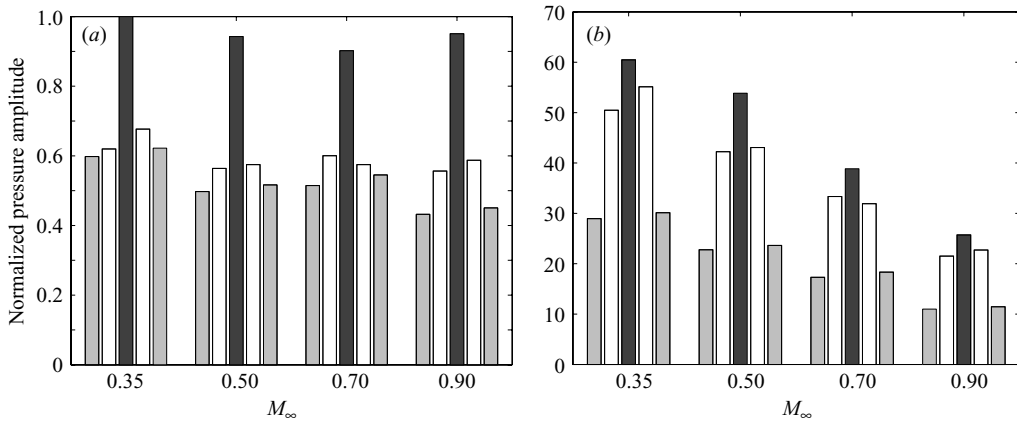


FIGURE 16. Balance of instability-wave amplitude (at $St = 0.35$ for cases A–D, unheated): (*a*) at the exit ($x/D = 0$); (*b*) at the peak. Pressure amplitude at $r/D = 0.5$ measured by the beam-forming is normalized by $\rho_\infty U_{jet}^2$, and the amplitude of the $m = 0$ mode for $M_\infty = 0.35$ at the exit is taken to be unity. Azimuthal modes of $m = -2, -1, 0, 1$ and $2$ are shown from left to right in each distribution.

exit. Its eigenvector in figure 15(*a*), however, cannot capture its mode-shape accurately because it must again satisfy the orthogonality condition with the first eigenvector.

### 5.3. *Compressibility effects*

To investigate the scaling of instability-wave amplitude with the Mach number, we first show the *azimuthal mode balance* for unheated jets at various values of $M_\infty$. We normalize all amplitudes by $\rho_\infty U_{jet}^2$ and then divide them by the amplitude of the $m = 0$ mode for case A at the nozzle exit (we use $\rho_\infty$ to normalize the azimuthal mode balance to readily compare with the far-field sound pressure level throughout this paper). The variation in azimuthal mode balance with the Mach number is displayed at the nozzle exit in figure 16(*a*) and the peak value along the mixing layer ($r/D = 0.5$) in figure 16(*b*) (actual pressure amplitudes are also given in table 3 in Appendix C).
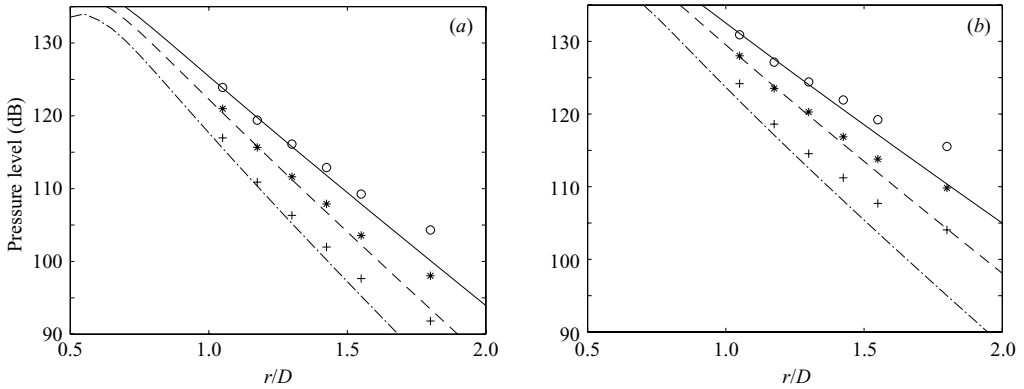
FIGURE 17. Pressure levels as a function of a radius at two different Mach numbers. Ring-wise pressure amplitudes and the eigenfunctions are compared (at $St = 0.35$ and $x/D = 2.5$): (a) case B ($M_\infty = 0.5$); (b) case D ($M_\infty = 0.9$). Notation is the same as figure 11.

The amplitudes at the nozzle exit demonstrate that the normalized disturbance level is nearly constant with the Mach number, which is consistent with the observation by Armstrong & Michalke (1977). In contrast, the peak pressure amplitude is substantially reduced with increasing Mach number, following the trends of growth rates predicted by the linear stability theory (Blumen 1970) (we should note, however, that significant deviation from the $U_{jet}^8$ scaling law has not been observed in the far-field sound pressure level by previous experiments, e.g. Tanna 1977). This also confirms the validity of the proposed detection algorithm: the magnitude determined from the detection algorithm appears to provide the appropriate amplitude at the nozzle exit, although the ring-wise data deviate from the eigenfunctions at the most upstream ring owing to resonance (refer to Appendix B or figure 18a).

Next, we consider the impact of the Mach number on the radial decay of pressure fluctuations. In figure 17, we compare pressure fluctuations for six different array positions at two different Mach numbers. At a higher Mach number (case D, $M_\infty = 0.9$), intensity of the acoustic signals relative to the hydrodynamic disturbances increases for all three modes. As a result, the outer edge of the linear hydrodynamic region shrinks. Yet, we can confirm that the third microphone position from the centre still appears to be appropriate. As the jet velocity increases, pressure amplitude associated with sound follows $\sim U_{jet}^4$ in the far field (Lighthill 1952), as opposed to $\sim U_{jet}^2$ in the linear hydrodynamic field. This implies, for example, that the pressure level in the near field can increase up to 10 dB from cases B to D, while the sound pressure level can increase as much as 20 dB in the far-field asymptote. The difference between figures 17(a) and 17(b) falls within this range, although it is less than the prediction because of the relatively small radial distance.

## 5.4. Temperature effects

Finally, to study the effects of the temperature ratio, we focus on $St = 0.30$, since the most unstable frequency tends to be lowered in heated jets. Figure 18 depicts the streamwise evolution of the pressure amplitude for unheated and heated cases at $M_\infty = 0.9$. Compared with the unheated jet, the axisymmetric mode is greatly amplified, while the other two modes are only slightly enhanced in the heated jet. All three modes saturate more rapidly, which is consistent with the shortened potential
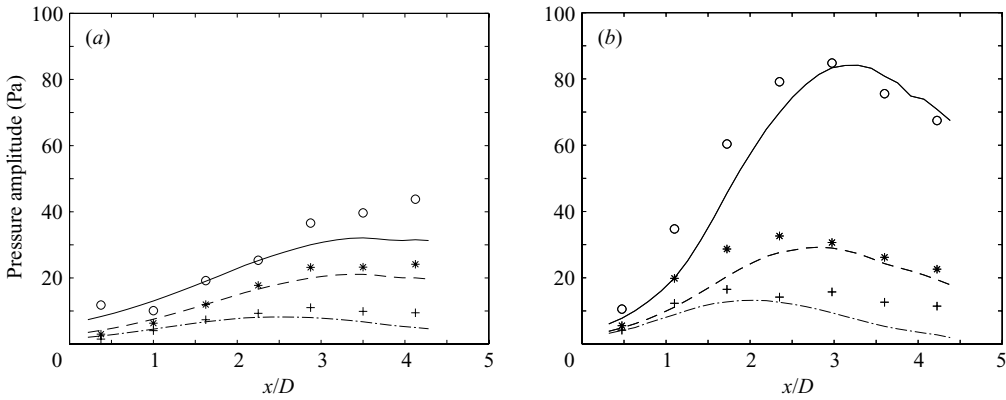
FIGURE 18. Evolution of pressure amplitude along the microphone array at different temperature ratios ($St = 0.30$ and $M_\infty = 0.9$): (a) case D (unheated); (b) case H ($T_{jet}/T_\infty = 2.70$). Notation is the same as figure 12.
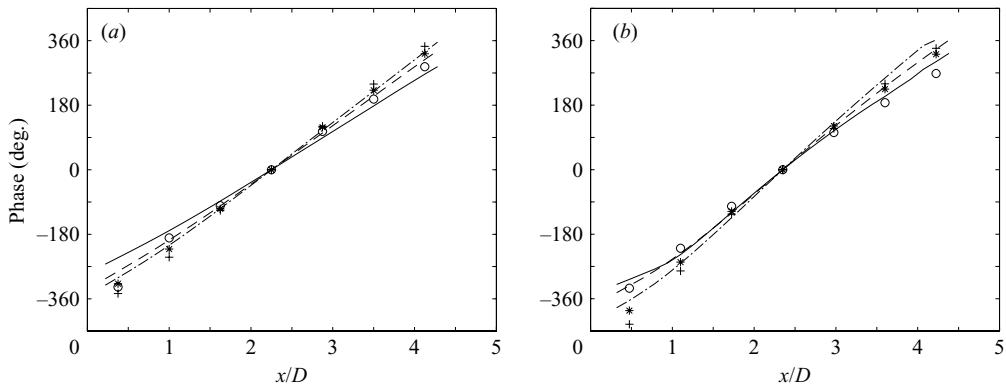


FIGURE 19. Averaged phase correlation along the microphone array at different temperature ratios. Flow conditions are the same as figure 18: (a) case D; (b) case H. Notation is the same as figure 12.

core in heated jets (Bridges & Wernet 2003). The averaged phase correlation is also plotted in figure 19. In contrast, the local wavenumber is nearly unchanged with temperature; namely, the phase speed is independent of the jet temperature.

The strong growth of the axisymmetric mode in heated jets can also be seen from the instability mode balance. Normalized azimuthal mode balance at the peak for $M_\infty = 0.9$ is displayed in figure 20(a). The amplification of $m = \pm 1$ and $\pm 2$ seems independent of the jet temperature, while $m = 0$ is noticeably enhanced with increasing temperature. At a lower Mach number ($M_\infty = 0.5$), the enhancement of the axisymmetric mode is even more amplified, as shown in figure 20(b). The phase correlation along the array is unchanged between cases B, E and G (not shown). For reference, the peak pressure amplitudes measured in this study are given in table 4.

Note that Tanna (1977) reported that at low Mach numbers (i.e. $M_\infty < 0.7$), the far-field sound pressure level near the peak frequency increases monotonically with increasing jet temperature, although the jet velocity relative to the ambient is the same. The experiments by Bridges & Wernet (2003) also confirmed the same trend with an
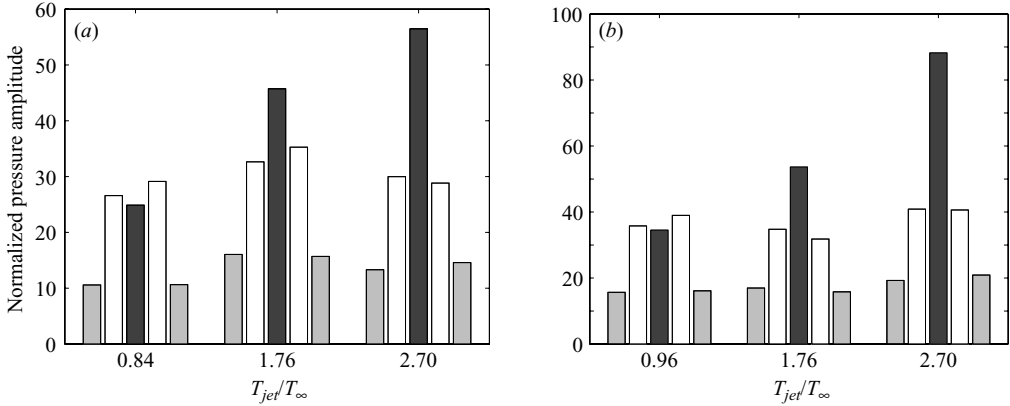
FIGURE 20. Balance of instability-wave amplitude at the peak for different temperature ratios (at $St = 0.30$). (a) $M_\infty = 0.9$ (cases D, F and H). (b) $M_\infty = 0.5$ (cases B, E and G). Pressure amplitude of $m = 0$ for the unheated case at $(x/D, r/D) = (0, 0.5)$ is taken to be unity. Notation is the same as figure 16(b).

approximately 8 dB increase from the unheated to $T_{jet}/T_\infty = 2.7$ cases at $M_\infty = 0.5$ over a wide range of polar angles. These experiments have also shown that at $M_\infty \gtrsim 0.7$, the dependence of the sound pressure level on the jet temperature becomes significantly weaker (the variation between the unheated and $T_{jet}/T_\infty = 2.7$ cases is within 3 dB at $M_\infty = 0.9$). On the other hand, we did not observe a substantial compressibility effect on instability wave amplitudes (see figure 20) as well as their phase speed in the near field. However, such trends in the far field are not simply related to the instability wave mode balance (even if the acoustic radiation were a linear process), since the radiative efficiency is also a function of the instability wave envelope (Crighton & Huerre 1990). Thus, we should not view the apparently conflicting trends between near and far field as supporting or conflicting with the hypothesis that instability waves are an important source of sound at low frequencies. This is discussed further in the conclusions.

## 6. Conclusions

We have developed an algorithm that detects instability waves in a subsonic turbulent round jet by measuring pressure on a conical surface just outside the mixing layer. The algorithm is analogous to the beam-forming technique; namely, it minimizes the least-squares norm between the pressure measured with a hydrodynamic array and the eigenfunctions from linear stability analysis. We have used a DNS database to set the initial design for the array; subsequently, we have optimized the microphone distribution by focusing on the frequency range from $St = 0.25$ to $0.50$ for the axisymmetric and first two azimuthal modes. The proposed algorithm has then been examined by experiments that cover a range of Mach numbers ($M_\infty = 0.35$ to $0.90$) and temperature ratios ($T_{jet}/T_\infty = 0.84$ to $2.70$).

For the experiments, we have compared radial decay and streamwise evolution between the amplitudes directly obtained from Fourier transforms (in time and the azimuthal direction) and the eigenfunctions whose amplitudes are determined by the proposed algorithm. We have also compared phase correlation between the first eigenvector of the cross-spectral matrix (i.e. the POD mode with the greatest

eigenvalue) and the linear stability theory. The comparisons have shown that there is an extensive region in the radial direction where linear hydrodynamic waves dominate the pressure field, and the deviations from the predicted eigenfunctions are generally within 2 dB over a range of frequencies ($St = 0.25$ to $0.50$). The agreement is particularly good near the most amplified frequency in each azimuthal mode ($m = 0$, $\pm 1$ and $\pm 2$).

The results of this study show that the influence of the compressibility and the temperature ratio on the instability-wave amplitude including their mode balance at the nozzle exit is relatively small. Moreover, the good agreement between the experimental data and the prediction may well indicate that the influence of small-scale turbulence on large-scale structures are negligible up to the end of the potential core, even for natural jets. Therefore, the growth rates of instability waves, which are predictable with linear stability analysis, govern the peak mode balance of the large-scale flow structures. We should note, however, that during any sampling period, pressure signals follow the eigenfunctions in a region less than two wavelengths in the streamwise extent; thus, the linear stability theory captures large-scale structures only in a statistical sense.

Despite the excellent agreement for the most amplified frequency of the near field, the growth rates near the nozzle exit tend to be under-estimated by the linear stability analysis at off-peak frequencies. The discrepancy is most severe for the axisymmetric mode ($m = 0$) at low frequencies where the governing length scale is changed from the local vorticity thickness to the jet diameter. It should be remembered that the linear stability analysis in this study assumes that the growth rate can be locally determined by the velocity and temperature profiles at each cross-section. As the axial wavelength of instability waves becomes longer at low frequencies, this assumption probably fails. Thus, the effect of the spreading mixing layer may cause the discrepancy, although the precise mechanism cannot be determined from the present study. To measure the instability wave amplitude for $m = 0$ at low frequencies, an accurate model must be developed as a reference solution for the beam-forming.

While the evidence presented here strongly supports the connection of linear instability waves evolving in the time-averaged flow field to the evanescent pressure field measured just outside the mixing layer, the connection to the far-field sound is less clear. When instability waves convect supersonically, they give rise to Mach wave radiation that has been clearly detected in previous experiments; certain aspects of their spectrum and directivity follow directly from linear stability theory. In contrast, for subsonically convecting waves (including the present experiments), models for their acoustic radiation have long been sought (Liu 1974; Fuchs & Michel 1978; Tam & Morris 1980; Mankbadi 1985; Zaman 1986; Crighton & Huerre 1990; Goldstein & Leib 2005), but their relevance to the observed acoustic field is still a topic of debate.

The present data, together with acoustic data acquired in the same facility and at the same conditions (J. Bridges & S.-S. Lee, personal communication 2004), offer an extensive database with which to explore the connections between instability waves and sound. For example, Reba *et al.* (2005) used a Green's function solution to the linear wave equation to project the present near-field array data to the far field and compared the results with the aforementioned far-field measurements. They showed that at polar angles of about $50°$, there was quantitative agreement between the projected near-field data and the far-field measurements, partly supporting a direct (linear) relation between instability waves and the far-field sound. Unfortunately, at smaller polar angles, the agreement was unsatisfactory, especially in those cases where truncation of the array near the end of the potential core caused a significant clipping

of the instability wave packets (cf. figure 18*a*). It appears that refraction, which is not accounted for in the Green's function, may also have contributed to the disagreement at shallow angles. In the future, we plan to further investigate the relation between instability waves and acoustic radiation using these datasets.

We have compared the proposed detection algorithm with a POD analysis of the experimental data. The POD extracts correlated structures based on their amplitude without assuming a form of the structures. The first POD mode gives almost perfect agreement with the linear stability theory for the phase correlation. On the other hand, it captures only a limited extent of the instability-wave envelope near the saturated region, because the characteristic length occupied by instability waves during a sampling interval is shorter than the length of the array. As a result, the upstream components of instability waves consist of multiple POD modes. On the other hand, the POD method can detect structures other than instability waves. An example from our study is upstream-propagating acoustic waves in the jet core, which may be important as a feedback mechanism. Once the physics of such a mode is identified and the structure is explicitly formulated, its amplitude could be determined accurately with the proposed technique. It should be remembered that the beam-forming algorithm gives the projection of signals onto the target mode that we wish to extract.

The optimal array position to extract linear hydrodynamic signals is a function of the frequency, while the number of microphones is generally limited. Therefore, the array configuration must be designed according to these requirements. For example, to measure instability waves at lower Strouhal numbers, the array must be extended in the axial direction; however, the assumption of the locally parallel mean flow probably fails beyond the end of the potential core. When we focus on higher Strouhal numbers or higher azimuthal modes, we must cluster microphones in the axial and the azimuthal directions, respectively. These measurements would require the use of smaller microphones so that the interaction with the entrained flow is minimized.

Detection algorithms based on least-squares optimization are being developed for a number of applications, including the detection of isolated vortices based on wall-pressure measurements (Suzuki & Colonius 2003), and the detection of trailing vortices from aircraft based on their ground-plane acoustic signature (Dougherty 2004). In addition, such detection algorithms can provide useful data for numerical simulations. For example, computational studies of turbulent jets suffer from incomplete information on the statistics of instability-wave amplitudes at the nozzle exit. The present data can provide such inflow conditions.

## Appendix A. Eigenfunction beyond the neutrally stable point

As Tam & Morris (1980) explained in their Appendix, we must consider carefully a branch-cut in the complex $r$-plane when we compute stable or neutrally stable eigenfunctions. As the velocity profile spreads downstream, the growth rates of
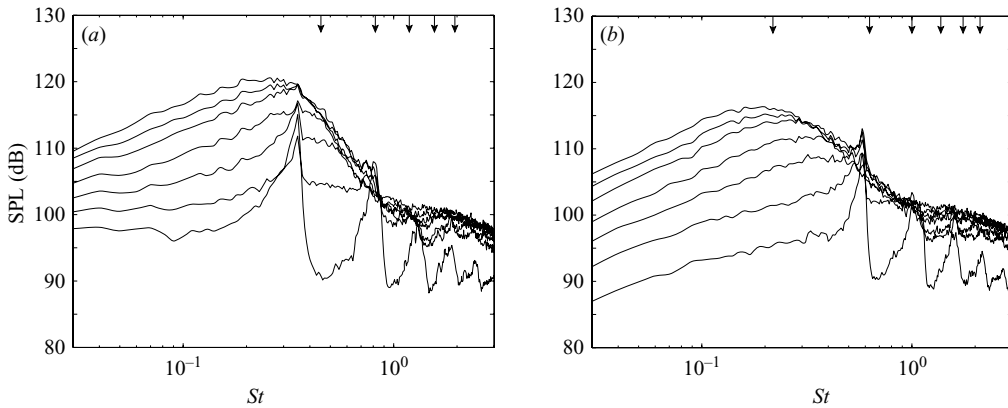
FIGURE 21. Frequency spectra in case D (at $M_\infty = 0.9$, unheated). Sound pressure levels of the first seven rings are plotted from the bottom: (a) $m = 0$; (b) $m = 1$. The arrows denote frequencies of duct-acoustic modes in a quiescent flow.

eigenfunctions vanish, i.e. $\text{Im}[k] = 0$, when $\omega - kU = 0$ at some $r$. This point is referred to as a *critical layer*, corresponding to a branch point in the complex $r$-plane. As the growth rate becomes negative further downstream, the imaginary part of the critical point in $r$ becomes positive. To circumvent this branch point, we integrate (2.2) along

$$r(\rho) = \rho + \mathrm{i}\Delta \exp\left[-\frac{(\rho - \text{Re}[r_*])^2}{\sigma^2}\right], \tag{A 1}$$

where $r_*$ satisfies $\omega - kU(r_*) = 0$. In this study, we use $\Delta/D = 0.04 + \text{Im}[r_*]$ and $\sigma/D = 0.02$ and integrate (2.2) in $0 \leqslant \rho \leqslant 3D$ by a shooting method (see Boyd 1985).

## Appendix B. Frequency spectra at high Mach numbers

In this experiment, we have observed a spurious resonance phenomenon, particularly at higher Mach numbers for unheated jets. Figure 21 depicts frequency spectra of the first seven rings from the nozzle exit (the data are Fourier-decomposed in the azimuthal direction) for case D ($M_\infty = 0.90$, unheated). In the $m = 0$ mode, the highest peak appears at $St \approx 0.35$, and their harmonics seem to follow at higher frequencies (although their spacings are not exactly harmonics). These peaks are smeared downstream. For $m = 1$, the spectra are first peaked at $St \approx 0.6$, and the qualitative characteristics are similar to those of the $m = 0$ mode. Note that the first peak frequency for $m = 2$ (not shown) is nearly the same as that of the second peak of the $m = 0$ mode. Thus, the first few rings are influenced for $m = 0$ in the frequency range of interest (from $St = 0.25$ to $0.50$).

This tonal sound is weaker or undetectable at lower Mach numbers or for heated jets. At $M_\infty = 0.7$ for an unheated case, the first peak is observed at $St \approx 0.6$ for $m = 0$; hence, it is not scaled with the Strouhal number (nor the Helmholtz number). Because six microphones at the same axial station were not directly tied in the array, this phenomenon is not caused by structural vibration. One hypothesis is that this signal originates from the internal aerodynamics. Here, we compute duct acoustic modes in a quiescent space, assuming that the wavelength in the axial direction is much longer than the rig radius (7.62 cm), and denote their Strouhal numbers by arrows

| | $M_\infty = 0.35$ | $M_\infty = 0.50$ | $M_\infty = 0.70$ | $M_\infty = 0.90$ |
|---|---|---|---|---|
| $m = -2$ | 97, 130 | 101, 135 | 107, 138 | 110, 138 |
| $m = -1$ | 97, 135 | 102, 140 | 109, 144 | 112, 144 |
| $m = 0$ | 101, 137 | 107, 142 | 112, 145 | 117, 146 |
| $m = +1$ | 98, 136 | 103, 140 | 108, 143 | 113, 145 |
| $m = +2$ | 97, 131 | 102, 135 | 108, 139 | 111, 139 |

TABLE 3. Pressure amplitude (dB) of instability waves. Values at the exit are listed on the left and those at the peak on the right (corresponding to figure 16).

| (a) | Unheated | $T_{jet}/T_\infty = 1.76$ | $T_{jet}/T_\infty = 2.70$ |
|---|---|---|---|
| $m = -2$ | 137 | 141 | 139 |
| $m = -1$ | 145 | 147 | 146 |
| $m = 0$ | 144 | 150 | 151 |
| $m = +1$ | 146 | 147 | 146 |
| $m = +2$ | 137 | 140 | 140 |

| (b) | Unheated | $T_{jet}/T_\infty = 1.76$ | $T_{jet}/T_\infty = 2.70$ |
|---|---|---|---|
| $m = -2$ | 132 | 132 | 133 |
| $m = -1$ | 139 | 139 | 140 |
| $m = 0$ | 139 | 142 | 147 |
| $m = +1$ | 140 | 138 | 140 |
| $m = +2$ | 132 | 132 | 134 |

TABLE 4. Pressure amplitude (dB) of instability waves at the peak. (a) Values at $M_\infty = 0.9$; (b) values at $M_\infty = 0.5$ (corresponding to figure 20).

in figure 21. The higher modes correspond to the harmonics in the radial direction (i.e. the Bessel functions). Although the first mode is absent in all cases (it is also the case for $m = 2$), the duct acoustic modes seem to scale the peak frequencies. Thus, the agreement partially supports the hypothesis. However, as mentioned above, this tonal sound is significantly suppressed at lower Mach numbers and for heated jets for unknown reasons; moreover, it is not observed in the far-field sound spectra. Hence, further investigation is required to fully understand this phenomenon.

Nevertheless, as discussed in §4.4, the error in amplitude determined by the proposed beam-forming algorithm is estimated to be of the order of 0.1 % even if this signal is perfectly correlated with instability waves. Moreover, from the study on the instability-wave amplitude at the nozzle exit over a range of Mach numbers, the influence of the resonance phenomenon is shown to be sufficiently small (see §5.3).

## Appendix C. Measured amplitudes of instability waves

The measured pressure amplitude of instability waves corresponding to figures 16 and 20 are given in tables 3 and 4, respectively.

### REFERENCES

ARMSTRONG, R. R. & MICHALKE, A. 1977 Coherent structures in jet turbulence and noise. *AIAA J.* **15**, 1011–1017.

ARNDT, R. E. A., LONG, D. F. & GLAUSER, M. N. 1997 The proper orthogonal decomposition of pressure fluctuations surrounding a turbulent jet. *J. Fluid Mech.* **340**, 1–33.

BLUMEN, W. 1970 Shear layer instability of an inviscid compressible fluid. *J. Fluid Mech.* **40**, 769–781.

BONNET, J. P., DELVILLE, J., GLAUSER, M. N., ANTONIA, R. A., BISSET, D. K., COLE, D. R., FIEDLER, H. E., GAREM, J. H., HILBERG, D., JEONG, J., KEVLAHAN, N. K. R., UKEILEY, L. S. & VINCENDEAU, E. 1998 Collaborative testing of eddy structure identification methods in free turbulent shear flows. *Exps. Fluids* **25**, 197–225.

BOYD, J. P. 1985 Complex coordinate methods for hydrodynamic instabilities and Sturm–Liouville eigenproblems with an interior singularity. *J. Comput. Phys.* **57**, 454–471.

BRIDGES, J. & BROWN, C. 2004 Parametric testing of chevrons on single flow hot jets. *AIAA Paper* 2004-2024.

BRIDGES, J. & WERNET, M. 2003 Measurements of the aeroacoustic sound source in hot jets. *AIAA Paper* 2003-3130.

BROOKS, T. F. & HUMPHREYS, W. M. 2003 Flap-edge aeroacoustic measurements and predictions. *J. Sound Vib.* **261**, 31–74.

BROWN, G. L. & ROSHKO, A. 1974 On density effects and large structure in turbulent mixing layers. *J. Fluid Mech.* **64**, 775–816.

CITRINITI, J. H. & GEORGE, W. K. 2000 Reconstruction of the global velocity field in the axisymmetric mixing layer utilizing the proper orthogonal decomposition. *J. Fluid Mech.* **418**, 137–166.

CRIGHTON, D. G. & GASTER, M. 1976 Stability of slowly diverging jet flow. *J. Fluid Mech.* **77**, 397–413.

CRIGHTON, D. G. & HUERRE, P. 1990 Shear-layer pressure fluctuations and superdirective acoustic sources. *J. Fluid Mech.* **220**, 355–368.

DOUGHERTY, R. P. 2002 Beamforming in acoustic testing. In *Aeroacoustic Measurements* (ed. T. J. Mueller), pp. 62–97. Springer.

DOUGHERTY, R. P. 2004 Aircraft wake vortex measurements at Denver international airport. *AIAA Paper* 2004-2880.

DOUGHERTY, R. P. & STOKER, R. W. 1998 Sidelobe suppression for phased array aeroacoustic measurements. *AIAA Paper* 98-2242.

FREUND, J. B. 2001 Noise sources in a low-Reynolds-number turbulent jet at Mach 0.9. *J. Fluid Mech.* **438**, 277–305.

FUCHS, H. V. & MICHEL, U. 1978 Experimental evidence of turbulent source coherence affecting jet noise. *AIAA J.* **16**, 871–872.

GOLDSTEIN, M. E. & LEIB, S. L. 2005 The role of instability waves in predicting jet noise. *J. Fluid Mech.* **525**, 37–72.

GRAMANN, R. A. & MOCIO, J. W. 1995 Aeroacoustic measurements in wind tunnels using adaptive beamforming methods. *J. Acoust. Soc. Am.* **97**, 3694–3701.

HALL, A., PINIER, J. & GLAUSER, M. N. 2006 Identifying the most energetic modes of the pressure and velocity near-field region of a $M = 0.85$ axisymmetric jet. *AIAA Paper* 2006-0314.

JOHNSON, D. H. & DUDGEON, D. E. 1993 *Array Signal Processing – Concept and Techniques*. Prentice–Hall.

JORDAN, P., COIFFET, F., DELVILLE, J. & GERVAIS, Y. 2004 Acoustic-hydrodynamic interaction in the entrainment region of subsonic jet flow. *AIAA Paper* 2004-3020.

LIGHTHILL, M. J. 1952 On sound generated aerodynamically. 1. General theory. *Proc. R. Soc. Lond.* A **211**, 564–587.

LILLEY, G. M. 1974 On the noise from jet. *AGARD CP* **131**, 1–12.

LIU, J. T. C. 1974 Developing large-scale wavelike eddies and the near jet noise field. *J. Fluid Mech.* **62**, 437–464.

MAESTRELLO, L. & FUNG, Y.-T. 1979 Quasi-periodic structure of a turbulent jet. *J. Sound Vib.* **64**, 107–122.

MANKBADI, R. R. 1985 On the interaction between fundamental and subharmonic instability waves in a turbulent round jet. *J. Fluid Mech.* **160**, 385–419.

MANKBADI, R. R. & LIU, J. T. C. 1981 A study of the interactions between large-scale coherent structures and fine-grained turbulence in a round jet. *Phil. R. Soc. Lond.* **298**, 541–602.

MATTINGLY, G. E. & CHANG, C. C. 1974 Unstable waves on a axisymmetric jet column. *J. Fluid Mech.* **65**, 541–560.

MICHALKE, A. & FUCHS, H. V. 1975 On turbulence and noise of an axisymmetric shear flow. *J. Fluid Mech.* **70**, 179–205.

MOHSENI, K., COLONIUS, T. & FREUND, J. B. 2002 An evaluation of linear instability waves as sources of sound in a supersonic turbulent jet. *Phys. Fluids* **14**, 3593–3600.

MORRIS, P. J., GIRIDHARAN, M. G. & LILLEY, G. M. 1990 On the turbulent mixing of compressible free shear layers. *Proc. R. Soc. Lond.* A **431**, 219–243.

MOSHER, M. 1996 Phased arrays for aeroacoustic testing: theoretical development. *AIAA Paper* 96-1713.

PETERSEN, R. A. & SAMET, M. M. 1988 On the preferred mode of jet instability. *J. Fluid Mech.* **194**, 153–173.

PIET, F. J. & ELIAS, G. 1997 Airframe noise source localization using a microphone array. *AIAA Paper* 97-1643.

PRIDMORE-BROWN, D. C. 1958 Sound propagation in a fluid flowing through an attenuating duct. *J. Fluid Mech.* **4**, 393–406.

REBA, R., NARAYANAN, S., COLONIUS, T. & SUZUKI, T. 2005 Modeling jet noise from organized structures using near-field hydrodynamic pressure. *AIAA Paper* 2005-3093.

SUZUKI, T. & BUTLER, G. W. 2002 New beam-forming algorithm for high speed jet flows. *AIAA Paper* 2002-2505.

SUZUKI, T. & COLONIUS, T. 2003 Inverse-imaging method for detection of a vortex in a channel. *AIAA J.* **41**, 1743–1751.

TAM, C. K. W. & MORRIS, P. J. 1980 The radiation of sound by the instability waves of a compressible plane turbulent shear layer. *J. Fluid Mech.* **98**, 349–381.

TAM, C. K. W. & MORRIS, P. J. 1985 Tone excited jets – Part V: A theoretical-model and comparison with experiment. *J. Sound Vib.* **102**, 119–151.

TANNA, H. K. 1977 Experimental-study of jet noise: 1. Turbulent mixing noise. *J. Sound Vib.* **50**, 405–428.

TANNA, H. K. & AHUJA, K. K. 1985 A research program at Lockheed on tone excited jets – Part I: Introduction. *J. Sound Vib.* **102**, 57–61.

TOLSTOY, A. 1993 *Matched Field Processing for Underwater Acoustics*. World Scientific.

UNDERBRINK, J. R. 2002 Aeroacoustic phased array testing in low speed wind tunnels. In *Aeroacoustic Measurements* (ed. T. J. Mueller), pp. 98–217. Springer.

VENKATESH, S. R., POLAK, D. R. & NARAYANAN, S. 2003 Beamforming algorithm for distributed source localization and its application to jet noise. *AIAA J.* **41**, 1238–1246.

ZAMAN, K. B. M. Q. 1986 Flow field and near and far sound field of a subsonic jet. *J. Sound Vib.* **106**, 1–16.

ZAMAN, K. B. M. Q. & HUSSAIN, A. K. M. F. 1980 Vortex pairing in a circular jet under controlled excitation. Part 1. General jet response. *J. Fluid Mech.* **101**, 449–491.